The Astronomical Journal, 171:354 (16pp), 2026 June https://doi.org/10.3847/1538-3881/ae4fba
© 2026. The Author(s). Published by the American Astronomical Society.
OPEN ACCESS

Methane on the Temperate Exo-Saturn TOI-199 b

Aaron Bello-Arufe[1], Renyu Hu[1,2,3,4], Mantas Zilinskas[1], Jeehyun Yang[1,5], Armen Tokadjian[1], Luis Welbanks[6], Guangwei Fu[7], Michael Greklek-McKeon[8], Mario Damiano[1], Jonathan Gomez Barrientos[9], Heather A. Knutson[9], David K. Sing[7,10], and Xi Zhang[11]

[1] Jet Propulsion Laboratory, California Institute of Technology, Pasadena, CA 91109, USA; aaron.bello.arufe@jpl.nasa.gov
[2] Department of Astronomy & Astrophysics, The Pennsylvania State University, University Park, PA 16802, USA
[3] Center for Exoplanets and Habitable Worlds, The Pennsylvania State University, University Park, PA 16802, USA
[4] Institute for Computational and Data Science, The Pennsylvania State University, University Park, PA 16802, USA
[5] The University of Chicago, Chicago, IL 60637, USA
[6] School of Earth and Space Exploration, Arizona State University, 781 Terrace Mall, Tempe, AZ 85287, USA
[7] Department of Physics & Astronomy, Johns Hopkins University, Baltimore, MD 21218, USA
[8] Earth and Planets Laboratory, Carnegie Institution for Science, Washington, DC 20015, USA
[9] Division of Geological and Planetary Sciences, California Institute of Technology, Pasadena, CA 91125, USA
[10] Department of Earth & Planetary Sciences, Johns Hopkins University, Baltimore, MD 21218, USA
[11] Department of Earth and Planetary Sciences, University of California Santa Cruz, Santa Cruz, CA 95064, USA
Received 2025 November 19; revised 2026 February 13; accepted 2026 February 28; published 2026 May 20

Abstract

Temperate ($T_{eq} < 400$ K) gas giants represent an unexplored frontier in exoplanet atmospheric spectroscopy. Orbiting a G-type star every ∼100 days, the Saturn-mass exoplanet TOI-199 b ($T_{eq} = 350$ K) is one of the most favorable low-temperature gas giants for atmospheric study. Here, we present its transmission spectrum from a single transit observed with JWST's NIRSpec G395M mode. Despite lower-than-nominal precision due to a pointing misalignment, the spectrum reveals the presence of CH_4 (Bayes factor of ∼700 in a cloudy atmosphere), corresponding to a metallicity of $C/H = 13^{+78}_{-12}\times$ solar, although the absence of detectable CO and CO_2 at the current precision disfavors metallicities $\gtrsim$50 × solar. We also tested several haze prescriptions (Titan-like tholin, soot, and water-rich tholin), but the preference for these models is weak (Bayes factors of ∼2 relative to the clear case). The spectrum also shows an increase in transit depth near 3 μm, which our self-consistent models attribute to either NH_3 or, less likely, HCN. Follow-up observations could distinguish between these species, helping determine the planet's vertical mixing regime. The TOI-199 system exhibits strong transit timing variations (TTVs) due to an outer non-transiting giant planet. For planet c, our TTV analysis reduces its mass uncertainty by 50% and prefers a slightly longer orbital period (but still within the conservative habitable zone) and higher eccentricity relative to previous studies. TOI-199 b serves as the first data point for studying clouds and hazes in temperate gas giants, with the detection of spectral features in its transmission spectrum indicating that temperate gas giants are promising targets for detailed atmospheric characterization.

Unified Astronomy Thesaurus concepts: Exoplanet atmospheric composition (2021); Extrasolar gaseous giant planets (509); G dwarf stars (556); James Webb Space Telescope (2291); Transit timing variation method (1710); Transmission spectroscopy (2133)

Materials only available in the online version of record: data behind figure, machine-readable table

1. Introduction

Hot Jupiters have dominated the landscape of atmospheric studies of exoplanets over the past two decades. Their frequent transits, large atmospheric scale heights, and favorable orbital geometry make them the most accessible exoplanets to characterize. These planets have been extensively observed with HST, Spitzer, and ground-based telescopes (e.g., H. A. Knutson et al. 2007; D. K. Sing et al. 2016; D. Ehrenreich et al. 2020), and more recently with JWST (e.g., L. Alderson et al. 2023; A. D. Feinstein et al. 2023), with recent milestones including the detection of quartz clouds and photochemically produced SO_2 in their atmospheres (D. Grant et al. 2023; S.-M. Tsai et al. 2023).

By contrast, low-temperature ($T_{eq} < 400$ K) transiting giants remain unexplored. A handful of these planets are known to transit their host stars, and some are highly suitable for atmospheric characterization via transmission spectroscopy. Many of these planets orbit G-type stars on long-period ($\gtrsim$100 days) orbits (e.g., L. Mancini et al. 2016; C. A. Beichman et al. 2018) and, unlike the vast majority of exoplanets probed with transit spectroscopy, they are not expected to be tidally locked (A. P. Showman et al. 2015). As a result, longitudinal temperature gradients in their atmospheres should be orders of magnitude smaller than for hot Jupiters.

At temperatures intermediate between those of Jupiter/Saturn and those of hot Jupiters, we expect to see unique manifestations of atmospheric chemistry. At $T_{eq} < 400$ K, CH_4 is the dominant carbon-bearing molecule, and a substantial fraction of nitrogen is expected to be in NH_3 (J. J. Fortney et al. 2020; R. Hu 2021; K. Ohno & J. J. Fortney 2023), with many low-temperature giant exoplanets also remaining warm enough to avoid H_2O condensation. This trait makes temperate gas giants ideal targets to measure the atmospheric abundances of C, N, and O and constrain their feeding zones and migration histories (e.g., K. I. Öberg et al. 2011; C. Mordasini et al. 2016;

Original content from this work may be used under the terms of the Creative Commons Attribution 4.0 licence. Any further distribution of this work must maintain attribution to the author(s) and the title of the work, journal citation and DOI.

M. Ali-Dib 2017; N. Espinoza et al. 2017; A. J. Cridland et al. 2019, 2020). Moreover, photochemical processes that drive hydrocarbon formation in the Jovian atmosphere (G. R. Gladstone et al. 1996; J. Moses et al. 2005) instead result in the formation of HCN over hydrocarbons in warmer gas giants (R. Hu 2021), with quantitative predictions depending on K_{zz} and chemical networks (S.-M. Tsai et al. 2021; X. Yu et al. 2021). The mechanisms to form HCN have been studied extensively for Titan (e.g., V. Vuitton et al. 2019), early Earth (e.g., V. Airapetian et al. 2016; P. B. Rimmer & S. Rugheimer 2019), and hot Jupiters (e.g., M. R. Line et al. 2011; Y. Kawashima & M. Ikoma 2018; R. Hobbs et al. 2019). Low-temperature giant exoplanets thus fill the temperature gap between Titan and hot Jupiters, and can provide valuable empirical constraints on the formation of HCN on the early Earth.

With a Transmission Spectroscopy Metric of 107, the newly confirmed planet TOI-199 b ($0.810 \pm 0.005\,R_J$, M. J. Hobson et al. 2023) stands out as one of the most favorable low-temperature giant planets for atmospheric characterization. Its mass and radius suggest a Saturn-like internal structure with an H_2-dominated atmosphere. The planet orbits its G9V host star every 105 days, receiving 2.5 times Earth's irradiation, which corresponds to a zero-albedo equilibrium temperature of 352 K. Its relatively low mass ($0.17 \pm 0.02\,M_J$) and eccentricity ($0.09^{+0.01}_{-0.02}$) suggest a low internal heat flux (J. J. Fortney et al. 2020) and further solidify TOI-199 b as a canonical test case for temperate giant exoplanets.

Here we present the first atmospheric reconnaissance of TOI-199 b from a single transit observed with JWST/NIRSpec G395M. Establishing TOI-199 b as the representative temperate gas giant for detailed atmospheric studies, this paper not only provides the initial constraints on its atmospheric properties, but also uses advanced atmospheric models to chart the next steps in the characterization. In addition, we analyze the JWST and TESS light curves to model the transit timing variations (TTVs) in the system, with the aim of refining the physical and orbital properties of the two known planets in the system, and predicting the transit times through to the end of the year 2040.

The paper is structured as follows. In Section 2, we describe our observations and our two independent data-reduction pipelines, and we present the resulting transmission spectrum. Section 3 reports the results from our two independent retrieval analyses. In Section 4, we present a series of self-consistent photochemical models anchored by the current data to delineate the current constraints and additional information about the planet's atmosphere that could be obtained with improved spectral precisions. In Section 5, we present the TTV analysis. Finally, in Section 6, we discuss the results and outline how future observations can be used to place constraints on the efficacy of vertical mixing and photochemistry in this archetype low-temperature giant exoplanet.

2. Observations and Data Reduction

As part of JWST's General Observer program 5177 (P.I. Hu), we observed a transit of TOI-199 b on Dec 23, 2024 UTC. We collected the data using the Near InfraRed Spectrograph (NIRSpec; S. M. Birkmann et al. 2022; P. Jakobsen et al. 2022) with the medium-resolution grating G395M ($R \sim 1000$), the SUB2048 subarray, and seven groups per integration.

According to the JWST Exposure Time Calculator (ETC), the TOI-199 system ($m_J = 9.3$) is bright enough to saturate the NIRSpec wide aperture target acquisition (WATA). We instead chose a nearby infrared source as the acquisition target. However, due to target acquisition failure, the nearby source fell outside the aperture during the observations, and instead the WATA found a noise peak of ~80 counts in the centroiding box (at least ~150 are typically required). As a result, our observations plausibly picked up the far wings of the point-spread function (PSF) of the science target or a diffraction spike. However, the differential nature of the transit measurement enabled us to still extract a useful transmission spectrum. The resulting spectral uncertainties are ~4–5× larger than predicted by PandExo (N. E. Batalha et al. 2017).

To ensure that our results are robust against different data treatment approaches, we performed two independent data reductions, which we detail below.

2.1. `Eureka!` Reduction

We reduced the data using version 1.1 of the `Eureka!` pipeline (T. Bell et al. 2022). `Eureka!` is structured into six stages: the first two stages calibrate the raw data; stage three performs optimal extraction; stages four and five generate and fit the lightcurves, respectively; and stage six displays the results. Our `Eureka!` setup was informed by prior applications to other NIRSpec datasets (M. Damiano et al. 2024; A. Bello-Arufe et al. 2025; R. Hu et al. 2025), but with modifications to minimize the noise in the resulting lightcurves and including additional steps to mitigate the systematics introduced by the failed WATA, all of which are described below.

Starting from the uncalibrated raw data in the NRS1 detector (i.e., the `*nrs1_uncal.fits` files), we ran stages one and two of `Eureka!`. These stages call a series of steps from the `jwst` pipeline (version 1.15.1, H. Bushouse et al. 2024) to perform initial processing and calibration. We ran all the default steps for NIRSpec time-series observations (TSO) data, except for the flat-field and photometric calibration steps. For the jump step, which identifies "up-the-ramp" outliers in each pixel, we increased the sigma threshold from the default value of 4 to a more conservative value of 7. To correct the superbias, we used the mean scale factor over all integrations. Prior to fitting the ramps, we performed group-level background subtraction using the average value in each detector column, excluding a region with a half-width of 8 pixels centered around the trace.

After calibration of the raw files, we ran `Eureka!`'s stage 3. Here, we extracted the detector columns 686–2044, which contain the spectral trace. We masked pixels with an odd data quality (DQ) entry, and we corrected the curvature of the trace by shifting each detector column by a whole number of pixels. To determine the position of the source, we fit a Gaussian function to each detector column. We applied another round of column-by-column background subtraction, this time using the average value of pixels located at least 9 pixels away from the center of the trace, with a 5σ threshold for outlier rejection. For the optimal extraction of the spectra (K. Horne 1986), we used an aperture with a half-width of 3 pixels and constructed the spatial profile using the median frame after clipping 5σ outliers and smoothing it with a window length of 13. We then masked three excessively noisy detector columns: 1488, 1661, and 1798.

In stage four, we generated spectroscopic lightcurves from 2.87 to 5.17 μm, with a bin size of $\Delta\lambda = 0.004\,\mu$m, which

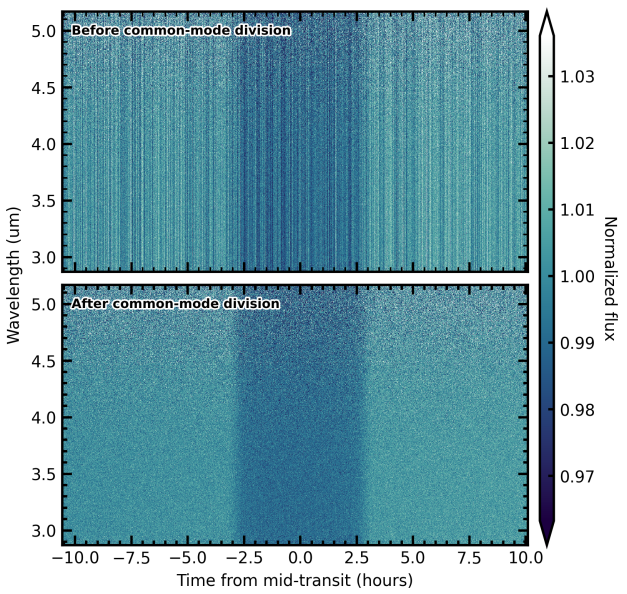


Figure 1. Raw spectroscopic lightcurves, as extracted with `Eureka!` and binned to $\Delta\lambda = 0.004$ μm, before and after dividing out the common-mode noise model.

closely matches the native spectral resolution of NIRSpec G395M ($R \sim 1000$). However, in order to test the robustness of our results against different binning schemes, we produced a second set of lightcurves at $\Delta\lambda = 0.025$ μm. We cleaned each lightcurve using a rolling boxcar filter with a width of 10 data points that recursively clipped 5σ outliers, up to 20 iterations.

The top panel in Figure 1 shows the raw spectroscopic lightcurves. While the transit of TOI-199 b is clearly visible around the middle of the observations, the lightcurves show wavelength-correlated noise. This systematic noise is caused by the failed WATA and, fortunately, is achromatic. As shown in Figure 1, we can effectively correct this noise by dividing out each spectroscopic lightcurve by a common-mode noise model.

To construct the common-mode noise model, we divided the white lightcurve by the best-fit model, which consisted of a `batman` transit model (L. Kreidberg 2015) multiplied by a systematics model (see e.g., F. Murgas et al. 2019; G. Fu et al. 2024). In our transit model, we fixed the period P, eccentricity e, and argument of periastron ω to the values reported by M. J. Hobson et al. (2023), and we assigned uniform priors to the remaining transit and orbital parameters, namely the planet-to-star radius ratio $R_p/R_\star$, the transit time T_0, the orbital inclination i_p, and the scaled semimajor axis $a/R_\star$. We also fitted for the quadratic limb-darkening coefficients (q_1, q_2, D. M. Kipping 2013), to which we assigned uniform priors between 0 and 1. Meanwhile, the systematics model consisted of a linear polynomial in time, and we also included a white noise multiplier to boost the error bars to match the scatter of the residuals. We performed the white lightcurve fits using the dynamic nested sampling package `dynesty` (J. S. Speagle 2020), which is included in `Eureka!`'s stage five. We used 2000 live points and set a convergence tolerance of $\Delta \log Z < 0.001$. The goal of this initial white lightcurve fit is solely to generate the common-mode noise model that is subsequently divided out from each spectroscopic lightcurve.

We then produced a second white lightcurve fit, which we used to report the system parameters and fix them in the spectroscopic lightcurve fits. One of the differences between this white lightcurve fit and the previous one is that our new systematics model additionally includes linear decorrelation against the x and y position and the width of the trace. This choice is motivated by an improvement in the Bayesian evidence. Another difference is that we now also include a step function to account for the jump in the y position (i.e., cross-dispersion direction) of the trace happening around the 6340th integration, right before egress (see Figure 2), which results in a jump in the lightcurve flux. Indeed, we found that linear decorrelation alone was not sufficient to account for the full extent of the jump in flux, and a Bayesian model comparison favors including a step function in the fits. We assigned a uniform prior to the step time and a normal prior centered around 0 to the step size. The third and final difference is binning of the lightcurve. The rms of the residuals decreases more steeply than the $N^{-1/2}$ scaling expected for uncorrelated noise, indicating the presence of high-frequency correlations (Figure 3, top panel). We binned the white lightcurve in time by a factor of 40 to mitigate these correlations, while still retaining sufficient points across the ingress and egress to accurately resolve the transit shape (Figure 3, middle panel). The prior and posterior system parameter distributions from this fit are presented in Table 1, and the best-fit model is shown in Figure 2.

To generate the transmission spectrum, we fitted the spectroscopic lightcurves in the same manner as the second white lightcurve fit, but with the following modifications. First, we kept T_0, i_p, and a/R_s fixed to the values listed in Table 1, but we still fitted for the quadratic limb darkening coefficients, independently for each channel. No temporal binning was applied to the spectroscopic lightcurves, since the RMS of the residuals behaves as expected for pure white noise after removing the common-mode signal (Figure 3, bottom panel). For computational reasons, we decreased the number of live points to 1000 and the convergence tolerance to $\Delta \log Z < 0.01$. To assess the impact of limb-darkening assumptions, we produced an additional reduction at $\Delta\lambda = 0.004$ μm with quadratic limb-darkening coefficients fixed to the values from the `ExoTiC-LD` package (D. Grant & H. R. Wakeford 2022), based on 3D stellar models (Z. Magic et al. 2015) and the stellar parameters from M. J. Hobson et al. (2023): $T_{\rm eff} = 5255$ K, $\log g = 4.582$, and [Fe/H] $= 0.22$. In total, we produced three reductions with `Eureka!`:

$\Delta\lambda = 0.004$ μm, with free limb darkening (our fiducial reduction).
$\Delta\lambda = 0.025$ μm, with free limb darkening.
$\Delta\lambda = 0.004$ μm, with fixed limb darkening.

2.2. `Tswift` Reduction

We performed an additional independent reduction of the NIRSpec dataset with the Transit swift routine (`Tswift`). The general steps are similar to those used in G. Fu et al. (2022). The default JWST pipeline is first used to process the `uncal.fits` files to produce the `darkcurrentstep.fits` files. Then the spectral trace is masked out, and the unilluminated regions are used to perform column-by-column $1/f$ and background subtraction at the group level. Next, we use the RampFitStep from the JWST pipeline to create the `rampfitstep.fits` files. Then, we cleaned the bad pixels and extracted the spectral trace. Because the source is outside the slit and we are capturing the flux of the PSF wings, the spectral

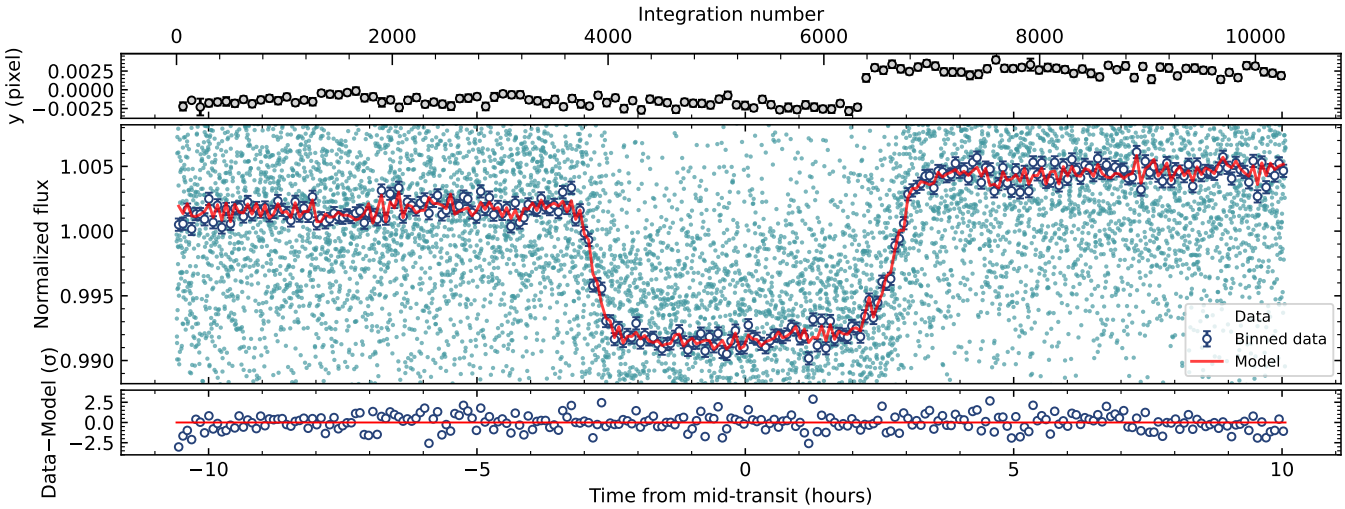


Figure 2. Top: mean-subtracted position of the trace along the y (i.e., cross-dispersion) direction, binned by a factor of 80 to more easily visualize the jump occurring right before egress. Middle: raw and binned ($\times$40) white lightcurves of TOI-199 b 's transit, observed with NIRSpec G395M, including the best-fit model, as extracted with `Eureka!`. Bottom: residuals from the best-fit model, measured in σ.

trace is broadened compared to typical observations. We decided to extract the spectra using a large aperture, with a width of 30 pixels along the spatial direction. Then each frame is summed in the vertical direction to create the white and spectroscopic lightcurves.

We also measured the spectral trace drift as a function of time and, as the `Eureka!` reduction, found a sudden small jump in the y direction around the 6340th integration, approximately 12.8 hr after the beginning of the observation (Figure 2). Due to the source being mostly outside the slit, this smaller drift in telescope pointing leads to significant wavelength-dependent slit-loss. To correct for this jump, we fitted a scaling factor for all points after the 6340th integration. So for the white lightcurve fit, we used `batman` (L. Kreidberg 2015) with eight total free parameters, including a linear slope, constant, R_p, a/R_s, inclination, mid-transit time, y-shift coefficient, and a scale factor for all points after the 6340th integration. Then we fixed the best-fit white light a/R_s, inclination, and mid-transit time values for the spectroscopic lightcurve fits while fitting for the remaining five parameters. The limb darkening parameters are fixed to the 3D Stagger-grid stellar models (Z. Magic et al. 2015). To check the robustness of fitting a scaling factor for all points after the 6340th integration, we also fit for the lightcurves with trimming all points after the 6340th integration. The resulting transit spectra from the two methods generally agree with a consistent shape. However, the trimming method results in larger error bars compared to the scaling factor approach due to the lack of egress and the subsequent baseline. The transit spectra from both methods are consistent with the one from `Eureka!`. In Figure 4, we compare the transmission spectra from the two independent reductions. Apart from a small vertical offset, the spectra show overall agreement.

3. Atmospheric Retrievals

We performed Bayesian atmospheric retrievals to interpret the transmission spectra. To assess the robustness of our results, we applied two independent codes: `ExoTR` (M. Damiano et al. 2024) and Aurora (L. Welbanks & N. Madhusudhan 2021).

3.1. ExoTR

`ExoTR`[12] is an atmospheric forward model and retrieval framework, which uses a nested sampling algorithm via `MultiNest` (F. Feroz et al. 2009) and `PyMultiNest` (J. Buchner et al. 2014) to statistically interpret exoplanet transmission spectra. `ExoTR` maps molecular mixing ratios to their observable signatures, and it includes the ability to model realistic water clouds, hazes, and stellar activity (M. Damiano et al. 2024). The framework has been applied across diverse targets—LHS-1140 b (cold, potentially water-rich), L 98-59 b (potentially volcanic), Kepler-51 d (a hazy super-puff), and K2-18 b (temperate sub-Neptune)—to infer atmospheric conditions from transmission data (M. Damiano et al. 2024; A. Bello-Arufe et al. 2025; R. Hu et al. 2025; J. E. Libby-Roberts et al. 2025).

We applied `ExoTR` to interpret the spectrum of TOI-199 b, fitting for a selected list of molecules and cloud parameters with uniform priors (Table 2), and with H_2 as the fill gas. The selection of the molecules in our canonical model was guided by insights from self-consistent atmospheric models (e.g., R. Hu 2021, and those developed in this work). The molecular opacities were calculated line-by-line using the most up-to-date line lists from HITEMP (R. J. Hargreaves et al. 2020; CH_4), ExoMol (J. Tennyson et al. 2016; SO_2), and HITRAN (I. E. Gordon et al. 2022; all other molecules). Both the opacity grid and the forward-model evaluation use a resolution of $R = 200{,}000$. Fixed parameters include the planet mass $M_p = 54.04\ M_\oplus$ and stellar properties (e.g., photospheric temperature of $T_s = 5255$ K; M. J. Hobson et al. 2023).

Figure 5 shows the best-fit model and molecular contributions from the retrieval. Many features are dominated by CH_4, especially in the 3.2–3.7 μm range; indeed, we are able to constrain CH_4 abundance to $\sim$1 dex and obtain a Bayes factor of 790, suggestive of a significant preference in favor of a model including CH_4 relative to a CH_4-free model. Other features are weakly fit with HCN, OCS, and/or CO_2 but these molecules, along with H_2O, NH_3, CO, SO_2, and H_2S, remain unconstrained. The 1D histogram for HCN and OCS suggests

[12] https://github.com/MDamiano/ExoTR

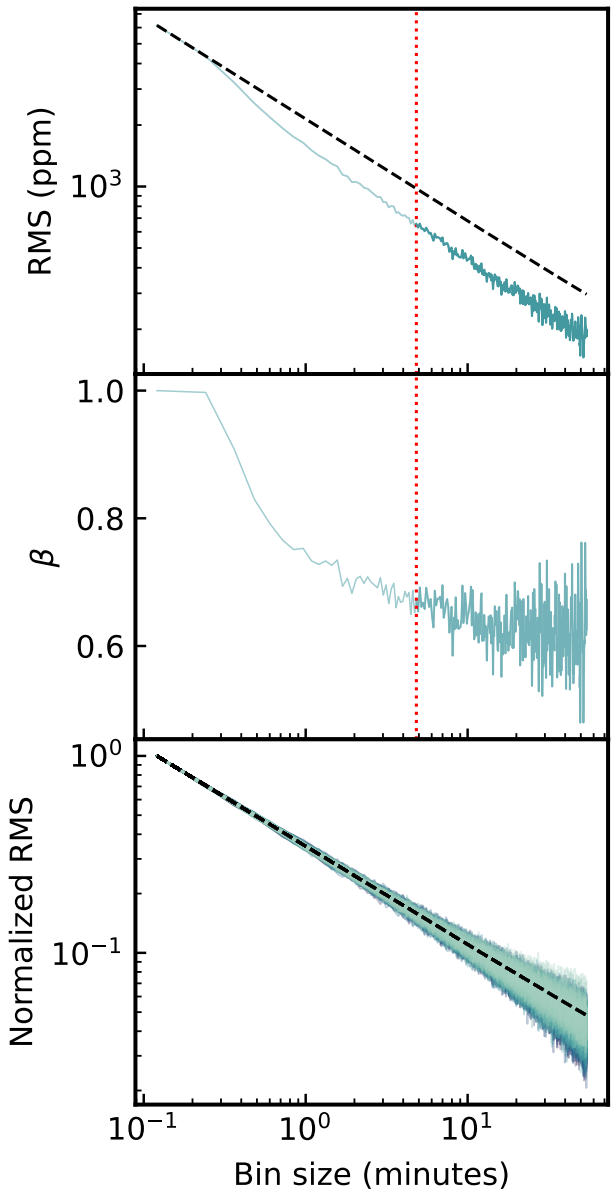


Figure 3. Top: RMS of the white lightcurve residuals as a function of bin size (solid teal line) and scaling expected for purely white noise (dashed black line). The dotted red line indicates the bin size used in the `Eureka!` white lightcurve fit (i.e., 40×). Middle: ratio of the two lines in the top plot (i.e., red noise factor, J. N. Winn et al. 2008). Bottom: normalized RMS of the residuals of the spectroscopic lightcurves from `Eureka!` as a function of bin size (solid colored lines) and scaling expected for purely white noise (dashed black line).

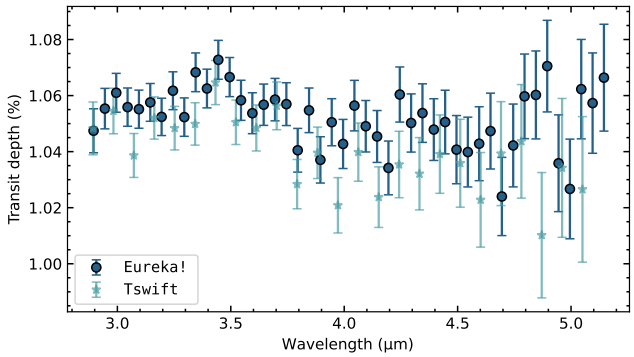


Figure 4. Comparison of the two independent reductions of the NIRSpec data of TOI-199 b.

(The data used to create this figure are available in the online article.)

Table 1
Prior and Posterior System Parameter Distributions for `Eureka!`'s White Lightcurve Fit

Parameter	Prior	Posterior
T_0 (BJD_{TDB}2 460 668)	$\mathcal{U}(0.15, 0.25)$	$0.21244^{+0.00039}_{-0.00039}$
i_p (°)	$\mathcal{U}(89.25, 90)$	$89.737^{+0.024}_{-0.021}$
a/R_s	$\mathcal{U}(50, 450)$	$119.1^{+3.0}_{-2.8}$
P (days)	104.854 (fixed)	104.854 (fixed)
e	0.09 (fixed)	0.09 (fixed)
ω	350 (fixed)	350 (fixed)
R_p/R_s	$\mathcal{U}(0.05, 0.15)$	$0.10268^{+0.00064}_{-0.00068}$
q_1	$\mathcal{U}(0, 1)$	$0.028^{+0.030}_{-0.016}$
q_2	$\mathcal{U}(0, 1)$	$0.29^{+0.39}_{-0.22}$

Note. $\mathcal{U}(a, b)$ is the uniform distribution between values a and b. The posterior values are reported as the median, with uncertainties given by the 16th and 84th percentiles.

a hint of their presence, but the wide tail toward low abundance weakens any claim of robustness. Table 2 highlights the 1σ confidence interval of the constrained species (CH_4) and the 2σ upper bounds for the unconstrained molecules.

We repeated the retrieval for three additional cases: the native spectral resolution data with fixed limb-darkening coefficients, data binned down to a resolution of 0.025 μm, and the data resulting from the `Tswift` reduction. Slight differences arise in the posterior solutions, but the main conclusions remain the same (see Figure 6).

We explored the effect of aerosols by repeating the baseline retrieval without the gray cloud, considering both a cloud/haze-free (clear) atmosphere and scenarios with a Mie-scattering haze, using optical properties of tholin (i.e., Titan haze analog, B. N. Khare et al. 1984), soot (i.e., absorbing black carbon, M. Hess et al. 1998), and organic haze (i.e., tholin-like aerosols experimentally produced in 400 K water-rich environments, C. He et al. 2024) individually to assess both the type and properties of hazes constrained by the data (see Figure 7). We found no significant preference between a cloudy and cloud-free model, with a Bayes factor of only 2.29 for clouds. The Bayes factors for hazy atmosphere models with tholin, soot, or organics are similarly small, suggesting ambiguity in the data for the presence of haze (Table 3). However, given the relationship between the atmospheric CH_4 and haze production, particularly for tholin and organics, we also test whether the evidence for haze increases for a CH_4-free model. Indeed, we find that the Bayes factor does not change for soot, which is simple carbon, but does increase significantly for tholin and organics (up to 35 and 36, respectively, or "very strong" evidence according to D. P. Thorngren et al. 2026). Thus, the evidence for CH_4 in a hazy atmosphere correspondingly decreases, from 291 to 22 and 16 for tholin and organics, respectively (and up slightly to 471 for soot). The haze particle diameters in these models are quite small (median of 0.015 μm) and the abundances are quite high (median of 40 ppm), suggesting that an unusually large cross section for haze is needed to make up for the lack of CH_4. Also, when comparing model evidence for CH_4 vs tholin/organic haze in analogous cases, there is always a

Table 2
Prior and Posterior Parameter Distributions from the ExoTR Fit to the Reference Eureka! Reduction

Parameter	Prior[a]	Posterior	Bayes Factor	Jeffreys Scale[b]
Planetary radius [R_p][c]	$\mathcal{U}(0.5, 2)$	$0.97^{+0.01}_{-0.02}$	…	…
Atmospheric temperature [K]	$\mathcal{U}(100, 500)$	325^{+88}_{-82}	…	…
Cloud top pressure [Pa]	$\mathcal{LU}(-1.0, 6.0)$	$2.3^{+1.4}_{-1.0}$	2.29	Barely worth mentioning
VMR H_2O	$\mathcal{LU}(-12, -0.3)$	<-2.05	1.07	Barely worth mentioning
VMR CH_4	$\mathcal{LU}(-12, -0.3)$	$-2.46^{+0.85}_{-1.15}$	790.16	Decisive evidence
VMR NH_3	$\mathcal{LU}(-12, -0.3)$	<-1.78	1.26	Barely worth mentioning
VMR HCN	$\mathcal{LU}(-12, -0.3)$	<-1.94	2.14	Barely worth mentioning
VMR CO	$\mathcal{LU}(-12, -0.3)$	<-3.55	0.95	Barely worth mentioning (against)
VMR CO_2	$\mathcal{LU}(-12, -0.3)$	<-3.47	1.15	Barely worth mentioning
VMR SO_2	$\mathcal{LU}(-12, -0.3)$	<-4.85	0.78	Barely worth mentioning (against)
VMR OCS	$\mathcal{LU}(-12, -0.3)$	<-3.12	2.75	Barely worth mentioning

Notes. For each species, we also report the Bayes Factor and corresponding Jeffreys interpretation, obtained by comparing the canonical model to a model excluding that parameter.
[a] $\mathcal{U}(a, b)$ and $\mathcal{LU}(a, b)$ are the uniform and log-uniform (Jeffreys) distributions between values a and b, respectively. Posteriors: median values with 1σ uncertainties. In the case of gases for which we did not obtain a detection, we present the upper limits corresponding to 95% (2σ) cumulative probability levels.
[b] H. Jeffreys (1939). Interpretations labeled "against" indicate that the data favor models excluding that parameter (i.e., Bayes factor <1).
[c] M. J. Hobson et al. (2023).

preference for the CH_4 model by a factor of ∼8. Since the presence of CH_4 is directly related to tholin and organic hazes, whether one model is preferred over the other does not change our main conclusion that there is strong evidence for CH_4 in the atmosphere of TOI-199 b. We also note that the mixing ratio of CH_4 remains nearly constant across all haze and gray cloud models, with a maximum difference in the median abundances of $\Delta \log(CH_4) = 0.28$, well below the 1σ uncertainties. To more rigorously constrain the presence or absence of clouds and hazes, additional transit data, especially at shorter wavelengths where a haze slope would be more prominent, would be especially helpful and would help to distinguish between a cloudy, clear, and hazy atmosphere.

3.2. Aurora

Aurora (L. Welbanks & N. Madhusudhan 2021) is a Bayesian retrieval and forward-modeling framework for interpreting exoplanet transmission and emission spectra (e.g., T. J. Bell et al. 2023; L. Welbanks et al. 2024). It solves the radiative transfer equation in a plane-parallel geometry under hydrostatic equilibrium, with flexible parameterizations of the atmospheric temperature structure, composition, and cloud/haze properties. Using this complementary framework, we tested the dependence of the retrieved atmospheric properties on the specific model assumptions considered in the main analysis from ExoTR in Section 3.1. This approach allows us to assess how model degeneracies (e.g., L. Welbanks & N. Madhusudhan 2019, 2022) and model construction choices (e.g., L. Welbanks et al. 2026) affect the interpretation of the atmospheric spectrum. Parameter estimation was performed using MultiNest (F. Feroz et al. 2009) via PyMultiNest (J. Buchner et al. 2014).

We explored three sets of modifications relative to the ExoTR baseline model to evaluate the robustness of retrieved CH_4, NH_3, and HCN abundances. Specifically, we considered (1) the relaxation of the isothermal temperature assumption, and (2) incorporating inhomogeneous cloud and haze cover. We performed retrievals using the model configurations described below on all reductions.

These atmospheric models considered the same absorbers as ExoTR (e.g., H_2O L. S. Rothman et al. 2010), CH_4 (S. N. Yurchenko & J. Tennyson 2014), NH_3 (S. N. Yurchenko et al. 2011), HCN (R. J. Barber et al. 2014), CO (L. S. Rothman et al. 2010), CO_2 (L. S. Rothman et al. 2010), SO_2 (D. S. Underwood et al. 2016), and OCS (J. S. Wilzewski et al. 2016). The opacities were computed line-by-line from the HITRAN (L. S. Rothman et al. 2010; C. Richard et al. 2012), HITEMP (R. J. Hargreaves et al. 2020), and ExoMol (J. Tennyson et al. 2016) databases, following the prescriptions in L. Welbanks & N. Madhusudhan (2021), and L. Welbanks et al. (2024).

Aurora accounts for the effects of inhomogeneous clouds and hazes modeled as a linear combination of a clear and cloudy/hazy region, following the cloud deck prescription and enhanced H_2-Rayleigh scattering described in L. Welbanks & N. Madhusudhan (2021), which builds upon the works of A. Lecavelier Des Etangs et al. (2008), M. R. Line & V. Parmentier (2016), and R. J. MacDonald & N. Madhusudhan (2017). For the non-isothermal temperature structure, we adopted the six parameter prescription from N. Madhusudhan & S. Seager (2009). All model spectra were computed at a resolving power of $R = 50{,}000$ over the wavelength range of 2.5–5.5 μm.

The retrieved spectra and posteriors from the analysis on the Eureka! reduction with $\Delta\lambda = 0.004$ μm are shown in Figure 8. For visual clarity, the shown data are binned. The retrieved atmospheric temperature structure is non-isothermal with $T = 494^{+283}_{-157}$ K at 100 mbar, which is consistent with the planet's equilibrium temperature at the 1σ level. The retrieved abundances of NH_3, H_2O, CO, CO_2, HCN, and OCS remain poorly constrained as with the analysis from ExoTR. However, the spectrum near ∼3 μm seems to be preferentially explained by the absorption line of NH_3 rather than clouds and HCN as with the ExoTR analysis. A model comparison between the model including the species and the model excluding it suggests no meaningful preference for the inclusion of NH_3.

Nonetheless, the interpretation of the spectrum of TOI-199 b as being largely explained by the methane feature at ∼3.3 μm and its broadband feature remains consistent. The retrieved CH_4 abundance is comparable with that derived from ExoTR,

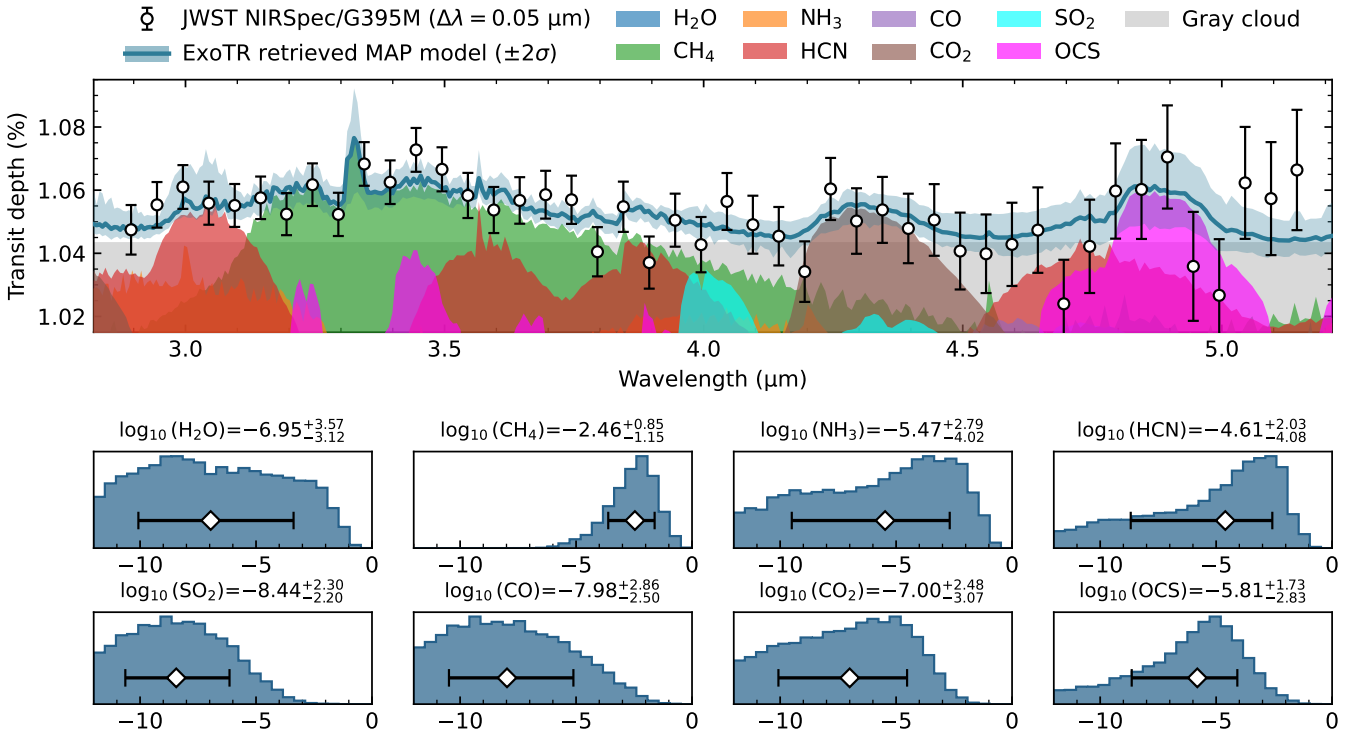


Figure 5. Top: maximum a posteriori (MAP) model and 2σ credible regions from ExoTR retrievals on the fiducial reduction, overlaid with data binned at $\Delta\lambda = 0.05$ μm. Also shown are the contributions from each molecule and clouds to the transmission spectrum. Bottom: 1D histograms of the posterior distributions from the retrieval results, including the median and $\pm1\sigma$ uncertainties (i.e., 16th and 84th percentiles).

although generally higher. This is consistent with expectations from known degeneracies between molecular abundances and the presence of inhomogeneous clouds/hazes (e.g., L. Welbanks & N. Madhusudhan 2019, 2021; M. C. Nixon et al. 2024). The preference for the model including CH_4 over the model without the absorber is marginally lower, with a Bayes factor of 705. The preference for the full over a model without NH_3 or without NH_3 and HCN is weak, with Bayes factors of 2. We emphasize that this model preference is relative to the specific set of molecules considered. Furthermore, including more species such as C_2H_6, C_2H_2, and C_2H_4, or other molecules considered in the full forward models (presented in Section 4), could alter the outcome (L. Welbanks et al. 2026).

4. Self-consistent Photochemistry Models

For a more in-depth exploration of the data, we now proceed to compare the NIRSpec G395M transmission spectrum of TOI-199 b against a series of self-consistent photochemical models at different metallicities, C/O ratios, internal temperatures, and vertical mixing efficiencies (K_{zz}). The first goal of this exercise is to determine whether the current data can place meaningful constraints on any of these parameters and evaluate the degree of agreement between the retrieval results and self-consistent photochemical models in radiative-convective equilibrium. The second goal is to identify the spectral regions where these parameters will make an appreciable difference and help identify future observation opportunities for TOI-199 b.

4.1. Model Setup

We modeled the atmosphere of TOI-199 b using the climate module of EPACRIS (R. Hu et al. 2024), previously applied in M. Damiano et al. (2024), J. Yang & R. Hu (2024a), and A. Bello-Arufe et al. (2025). We explored both solar and enhanced metallicity cases (M/H = 10) and considered solar (0.59) and super-solar (1.1) C/O ratios. While not shown, we find that increasing the C/O ratio to 1.1 has only a weak effect on the transmission spectrum. Because gas giants span a wide range of possible internal temperatures depending on mass, age, evolutionary history, and orbital eccentricity (J. J. Fortney et al. 2020), we examined models ranging from a nominal internal temperature of $T_{\rm int} = 50$ K up to 150 K. To explore the role of vertical mixing, we explored several eddy diffusion coefficient (K_{zz}) profiles (Figure B1), including the nominal profile with a K_{zz} of 10^6 cm^2 s^{-1} in the convective region and 10^8 cm^2 s^{-1} in the deep atmosphere (X. Zhang & A. P. Showman 2018), and a Jupiter-like profile with much weaker mixing in the convective region ($K_{zz} \sim 10^3$ cm^2 s^{-1}, G. R. Gladstone et al. 1996). We also explored uniform K_{zz} spanning 10^4–10^8 cm^2 s^{-1} as assumed by most hot-Jupiter studies, but we did not find significant deviations from the more realistic models. Further details of the self-consistent model setup are provided in Appendix B.

4.2. Self-consistent Model Results

Figure 9(a) compares solar and enhanced metallicity atmospheres. The main components (i.e., CH_4, NH_3, and H_2O) scale nearly linearly with metallicity. CH_4 and NH_3 remain within the observed uncertainty range at both solar and 10 × solar metallicity. While the deep-atmosphere abundance of HCN scales sharply with metallicity, its upper-atmosphere abundance is less affected as it is also governed by the balance between photochemical loss and vertical mixing (R. Hu 2021). The atmospheric abundance of CO and CO_2 scales nonlinearly with the metallicity, and metallicity

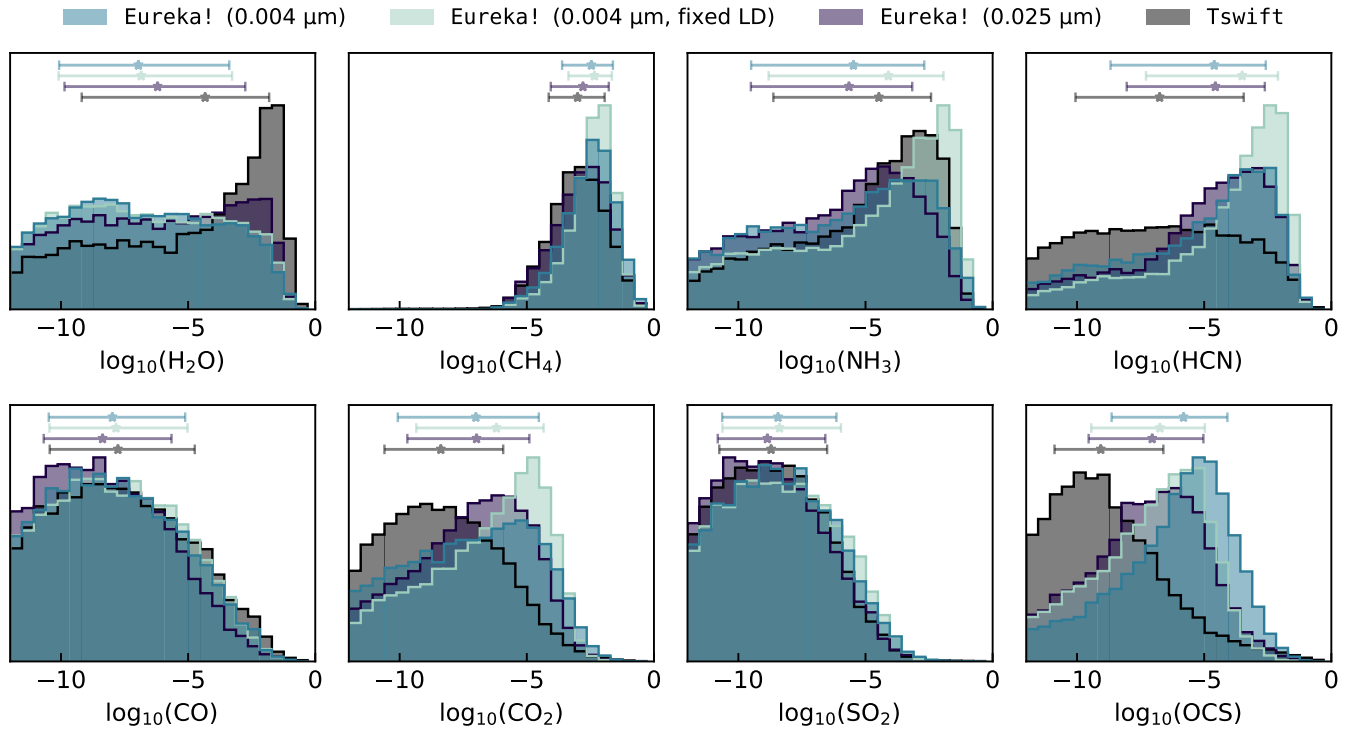


Figure 6. Posterior distributions of the gas abundances from the ExoTR retrievals on the different data reductions. Medians and 1σ uncertainties are overplotted as markers with horizontal error bars.

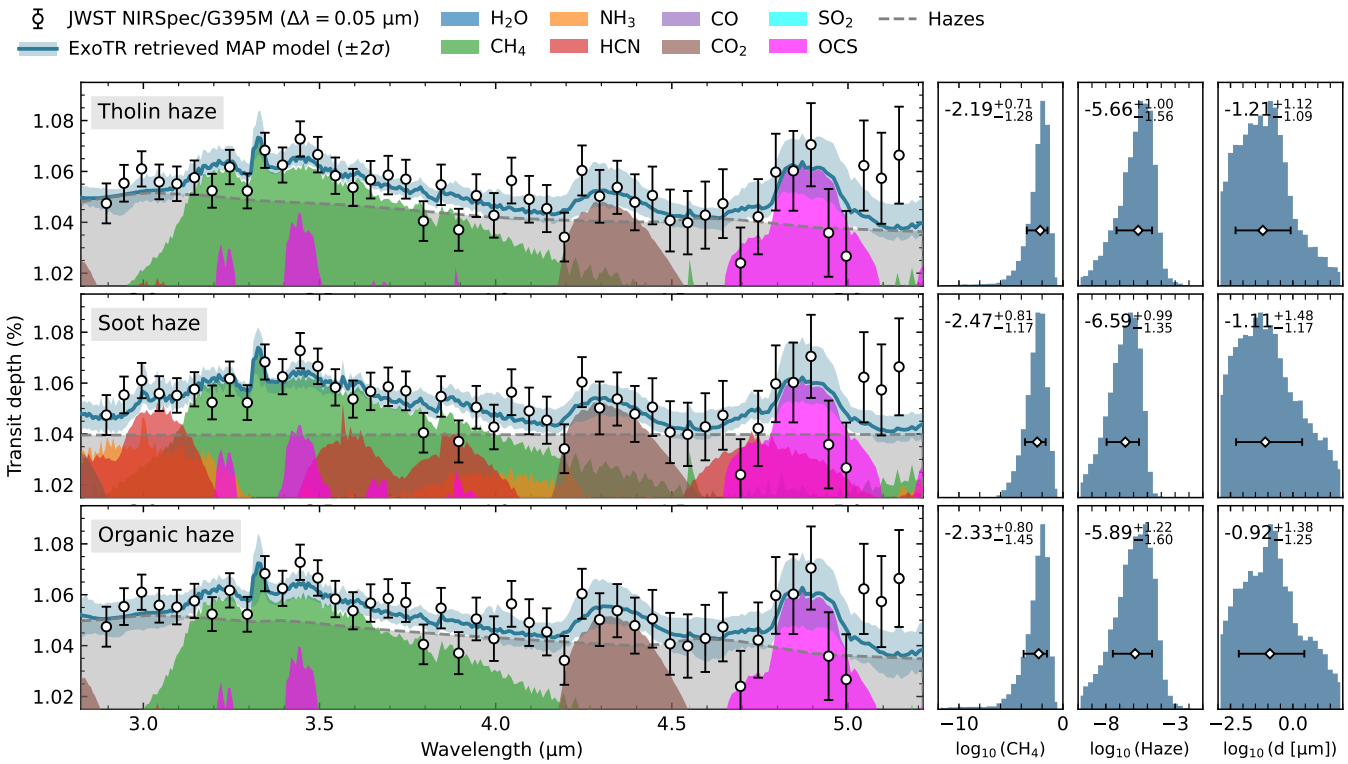


Figure 7. Same as Figure 5, but for models that include a tholin haze (top), a soot haze (middle), and an organic haze (bottom). Next to each spectrum we show the corresponding 1D histograms of methane and the haze abundance and particle diameter.

values larger than M/H = 10 push CO and CO_2 beyond the observed 2σ upper limits, making significantly higher metallicities unlikely for TOI-199 b.

Figure 9(b) shows a comparison of major photochemical abundances for an atmosphere with enhanced solar metallicity (M/H = 10) and nominal K_{zz} for internal temperatures of

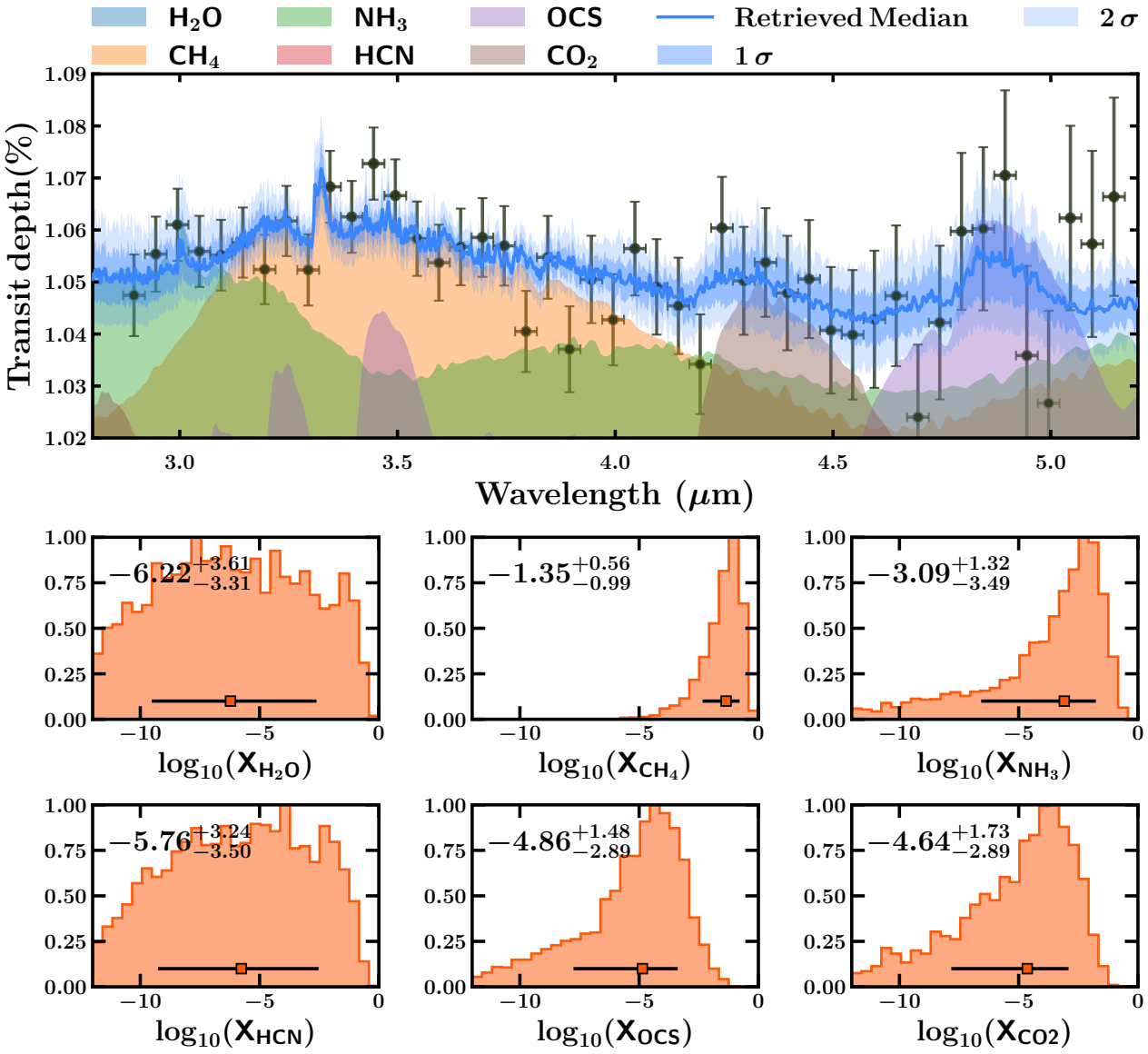


Figure 8. Top: best-fit spectrum with 1σ and 2σ model posteriors, from retrievals using Aurora and molecule contributions from the best fit model. Bottom: Posterior distributions for the molecules of interest, including the median and $\pm 1\sigma$ uncertainties.

Table 3
Bayes Factor (BF) for CH_4 and Various Haze Types from ExoTR Retrievals

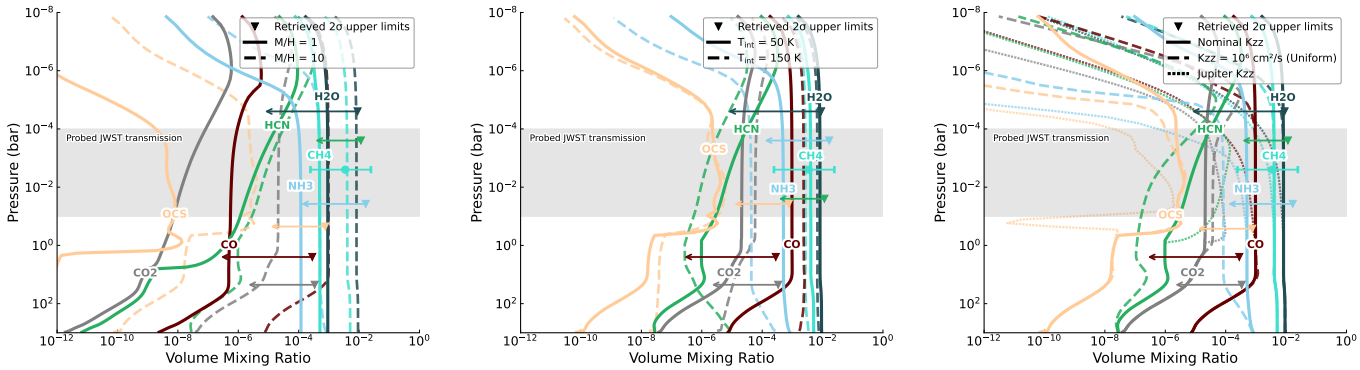
Baseline Case	BF(CH_4)	BF(Haze)	Ratio
clear, no CH_4	291	35 (tholin)	8.3
		36 (organics)	8.1
		1.6 (soot)	180
tholin w/CH_4	22.4	2.68	8.4
organics w/CH_4	16.1	2.00	8.1
soot w/CH_4	471	2.61	180

Note. For the first block, the baseline is a clear atmosphere with no CH_4. We report the Bayes factor for adding CH_4 versus adding each haze type individually. For the remaining three rows, the baseline contains both haze and CH_4, and we assess the Bayes factor by removing either the CH_4 or the haze, one at a time.

$T_{\rm int} = 50$ K and $T_{\rm int} = 150$ K. Increasing the internal temperature has important implications for the resulting composition: while CH_4 and H_2O remain the main carbon and oxygen carriers, CO increases substantially and nearly overtakes CH_4. Higher temperatures in the deep atmosphere also suppress NH_3, decreasing its VMR by approximately an order of magnitude. This also causes the abundance of HCN in the observable part of the atmosphere to decrease substantially, because HCN is derived photochemically from NH_3.

Figure 9(c) illustrates the impact of vertical mixing on atmospheric composition. For NH_3, a strong deep-atmosphere mixing ($K_{zz} = 10^8\,{\rm cm^2\,s^{-1}}$), which is assumed in the nominal and Jupiter-like cases, leads to quenching at higher pressures and results in atmospheric abundances reflective of the overall nitrogen abundance of the envelope. However, if K_{zz} is reduced to $10^6\,{\rm cm^2\,s^{-1}}$ in the deep atmosphere, NH_3 is quenched at $\sim$10 bar, resulting in a VMR decrease by a factor of 10 with respect to the $K_{zz} = 10^8\,{\rm cm^2\,s^{-1}}$ cases. Consequently, the abundance of HCN in the observable part of the atmosphere is also suppressed.

Between the nominal and Jupiter-like cases, the eddy diffusion coefficient K_{zz} in the convective region differs significantly, leading to substantial differences in the amount of HCN that accumulates in the observable atmosphere.



(a) Metallicity (b) Internal temperature (c) Eddy diffusion

Figure 9. Effects of key atmospheric parameters on the photochemical equilibrium abundances in TOI-199 b. (a) Comparison between solar and enhanced metallicity atmospheres, assuming a solar C/O ratio and $T_{\rm int} = 50$ K. Colored arrows denote the retrieved CH_4 abundance (1σ) from `ExoTR` and 2σ upper limits for other species, with arrow lengths indicating 1σ uncertainties. The gray shaded region marks the approximate pressure range probed in transmission. (b) Comparison between models with $T_{\rm int} = 50$ K and $T_{\rm int} = 150$ K, assuming enhanced metallicity ($M/H = 10$). (c) Comparison of various eddy diffusion (K_{zz}) profiles, assuming $M/H = 10$ and $T_{\rm int} = 50$ K.

Although HCN originates from similar NH_3 abundances, a bottleneck in vertical transport—such as in the Jupiter-like case, where K_{zz} is small in the upper troposphere—allows photochemically produced HCN to accumulate more efficiently in the upper atmosphere, resulting in a higher steady-state abundance (Figure 9(c)). Consequently, the HCN/NH_3 ratio in the observable atmosphere provides a sensitive diagnostic of the efficiency of vertical transport in the atmosphere of TOI-199 b.

4.3. Comparison to the Observations

Figure 10 shows the resulting transmission spectra from our self-consistent models, comparing several cases that highlight differences in spectral features caused by metallicity, internal heating, and vertical mixing efficiency. The best-fitting models from our set are the enhanced-metallicity cases ($M/H = 10$) with the Jupiter-like K_{zz} and a uniform $K_{zz} = 10^8\,{\rm cm^2\,s^{-1}}$ profile, both with a reduced chi-squared of $\chi^2_\nu = 1.0469$. However, due to the lower-than-expected precision in our program, all of the presented models can reasonably explain the observed transmission spectrum.

5. TTV Analysis

In order to refine the physical and orbital properties of the two known planets in the TOI-199 system and predict future transit times, we combined the JWST data with TESS observations to perform an updated TTV analysis. Planetary mass affects the transmission spectrum through the atmospheric scale height; however, as described below, the derived mass for TOI-199 b remains identical to that reported by M. J. Hobson et al. (2023). Consequently, the assumed scale height is unchanged and the atmospheric inferences are unaffected.

The strong TTVs in this system were first reported by M. J. Hobson et al. (2023), who performed a joint analysis between TTV and radial velocity data (RV) obtained by TESS and several ground-based observatories. This TTV+RV analysis revealed TTVs with a peak-to-peak amplitude around 60 minutes for TOI-199 b and suggested a non-transiting planet with an orbital period of ∼274 days and mass of $\sim 0.28\,M_{\rm J}$, placing it in the conservative habitable zone. The TOI-199 system is relatively uncommon in that it exhibits strong TTVs, but the two known planets are not near any first- or second-order orbital resonances, which are typically responsible for causing observed TTVs (e.g., Y. Lithwick et al. 2012; T. Holczer et al. 2016). In the case of TOI-199, the two massive planets on eccentric and close-in (<1 au) orbits dynamically perturb each other enough to cause large TTVs without proximity to resonance, which leads to TTVs that do not exhibit the typical sinusoidal pattern (e.g., E. B. Ford et al. 2012; K. M. Deck & E. Agol 2016, see also Figure 11).

Since the original publication of TTVs in the TOI-199 system in M. J. Hobson et al. (2023), three more transits of TOI-199 b have been observed in subsequent TESS sectors, including one additional transit prior to our scheduled JWST transit observation. We extracted transit times for TOI-199 b from TESS sectors 67, 87, and 94, using the same procedure as described in M. Greklek-McKeon et al. (2025b). In brief, this involved constructing a TESS photometric model using the `exoplanet` package (D. Foreman-Mackey 2018) for the transit lightcurve component, and a Matern-3/2 Gaussian Process (GP) kernel from `celerite2` (D. Foreman-Mackey et al. 2017) to model out-of-transit stellar variability. Our fits to the TESS data used 2 minutes cadence data from the Science Processing Operations Center pipeline (SPOC; J. M. Jenkins et al. 2016), which excluded ∼30% of data that was flagged by the SPOC pipeline for poor data quality, including a potential transit event in sector 90. A more careful photometric extraction from a custom TESS aperture, similar to the technique of M. J. Hobson et al. (2023), may be able to recover an additional transit event for TOI-199 b in future work. Our transit model includes parameters for the stellar radius $R_\star$, impact parameter b, scaled semimajor axis $a/R_\star$, planet-to-star radius ratio $R_p/R_\star$, and individual transit mid-center times to account for TTVs. The GP model includes a mean offset parameter μ and hyperparameters σ and ρ corresponding to the amplitude and timescale of quasiperiodic oscillations, along with an error scaling term added in quadrature to the TESS flux errors. We fixed the planetary eccentricities to zero in the transit fit, as in M. J. Hobson et al. (2023), since the corresponding effect on the transit lightcurve shape is negligible. We also fixed the quadratic limb-darkening parameters $u_1 = 0.466$ and $u_2 = 0.117$, as predicted by the

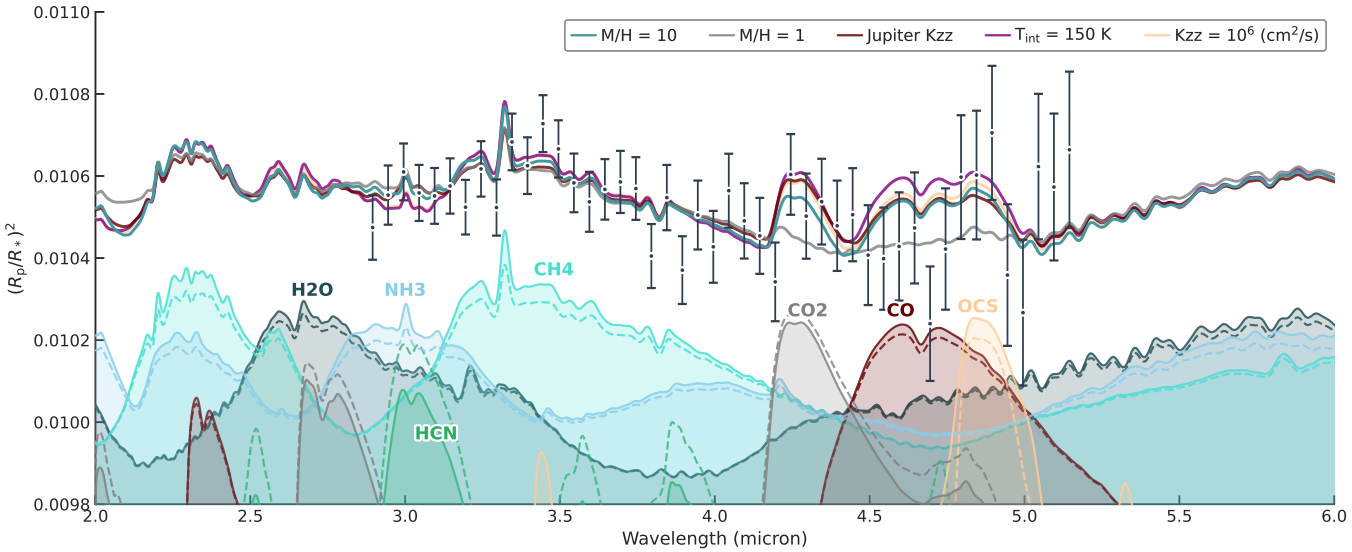


Figure 10. Self-consistent model transmission spectra comparison for TOI-199 b. The teal spectrum represents an enhanced metallicity case (M/H = 10) using the nominal K_{zz} profile. For enhanced metallicity, we also show spectra with a Jupiter-like K_{zz} profile (red), increased internal temperature (purple), and a uniform K_{zz} value of 10^6 cm^2 s^{-1} (orange). Additionally, the solar metallicity spectrum is shown in gray. Individual opacity contributions of the M/H = 10 model are shown via solid shaded regions. Individual contributions, shown in dashed lines, represent the Jupiter-like case. All spectra are offset to minimize χ^2. NIRSpec data are shown for the fiducial `Eureka!` reduction binned at $\lambda/\Delta\lambda = 100$ for visualization.

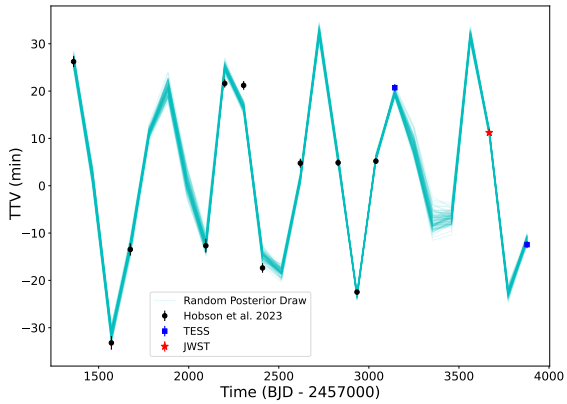


Figure 11. Observed TTVs for TOI-199 b from the M. J. Hobson *et al.* (2023) discovery paper (black points) and new data from JWST (red star) and TESS sectors 67, 87, and 94 (blue squares), along with 100 random draws from the best-fit TTV model (blue lines).

`ldtk` package (H. Parviainen & S. Aigrain 2015) using the stellar temperature, [Fe/H], and log g values reported in M. J. Hobson et al. (2023). We placed Gaussian priors on $R_\star$, b, $a/R_\star$, and $R_p/R_\star$ using the values reported in Tables 2 and 3 of M. J. Hobson et al. (2023), and placed a uniform prior on individual transit times ±12 hr from the transit time predicted from the M. J. Hobson et al. (2023) ephemeris. We used the `PyMC3` package (J. Salvatier et al. 2016) to sample the posterior distribution of our model with four parallel chains run with 2000 burn-in steps and 2000 posterior sample draws. We confirmed that the chains evolved until the Gelman–Rubin statistic values were <1.01 for all parameters, and that the transit mid-time posteriors were unimodal and normally distributed. The transit times from sectors 67, 87, and 94, along with the best-fit JWST transit time, and predicted transit times through 2040 December 31, are listed in Table 4.

Using the new TOI-199 b transit times, we performed an updated TTV fit following the procedure of M. Greklek-McKeon et al. (2025b). This involved using the TTVFast package (K. M. Deck & E. Agol 2016) to model the observed transit times listed in Table 4. The modeled transit times are a function of the planetary masses and orbital elements relative to a reference epoch at the TTV model start time, which we chose to be 1256.14 (BJD2457000) to match the simulation start time of M. J. Hobson et al. (2023). This simulation start time is close to one orbital period before the first observed transit of TOI-199 b, which can make TTV model convergence more difficult due to slight changes in the orbital period parameter for TOI-199 b altering the total number of transit events within the simulation time period, but we use this start time regardless for consistency with the M. J. Hobson et al. (2023) model.

In our TTV modeling, we fixed the planetary orbital inclinations to 90°and the stellar mass to 0.936 $M_\odot$, as in the original TTV analysis of M. J. Hobson et al. (2023). Our TTV model has ten free parameters in total, including: the planet-to-star mass ratios, average Keplerian orbital periods over the simulation period, initial mean anomalies (M_0) re-parameterized as the time of first transit (T_0), and the planetary eccentricities (e) and longitudes of periastron (ω). We re-parameterized the latter two quantities as $\sqrt{e}\cos(\omega)$ and $\sqrt{e}\sin(\omega)$ to mitigate the degeneracy between e and ω in our fits while retaining an effective uniform prior on e, as recommended by (J. Eastman et al. 2013). The orbital periods, mean anomalies, eccentricities, and longitudes of periastron are osculating orbital elements defined at the TTV model start time. We fit this model to the data using the MCMC ensemble sampler `emcee` (D. Foreman-Mackey et al. 2013), and chose wide uniform priors for all parameters (see Table 5) except the mass of TOI-199 b, for which we use a Gaussian prior derived from the independent RV mass constraint of M. J. Hobson et al. (2023), which is scaled from the RV semi-amplitude constraint.

We performed our TTV fit including the original transit times published in M. J. Hobson et al. (2023), the JWST transit time, and additional new TESS data from sectors 67, 87, and 94. The same TOI-199 b transit observed by JWST was also observed by TESS in sector 87, so we used the error-weighted average of these transit times along with its corresponding uncertainty in the TTV model. We initialized this TTV fit with 300 walkers (30 per

Table 4
Transit Times for TOI-199 b

Transit Time (BJD—2457000)	Source
$1361.0283^{+0.0008}_{-0.0008}$	H23
$1465.8841^{+0.0002}_{-0.0002}$	Predicted
$1570.7320^{+0.0010}_{-0.0010}$	H23
$1675.6182^{+0.0009}_{-0.0009}$	H23
$1780.5078^{+0.0009}_{-0.0011}$	Predicted
$1885.3868^{+0.0020}_{-0.0026}$	Predicted
$1990.2454^{+0.0019}_{-0.0025}$	Predicted
$2095.1087^{+0.0010}_{-0.0010}$	H23
$2200.0050^{+0.0006}_{-0.0006}$	H23
$2304.8772^{+0.0006}_{-0.0006}$	H23
$2409.7229^{+0.0007}_{-0.0007}$	H23
$2514.5948^{+0.0051}_{-0.0059}$	Predicted
$2619.4833^{+0.0007}_{-0.0007}$	H23
$2724.3750^{+0.0040}_{-0.0050}$	Predicted
$2829.2283^{+0.0005}_{-0.0005}$	H23
$2934.0818^{+0.0003}_{-0.0003}$	H23
$3038.9735^{+0.0004}_{-0.0004}$	H23
$3143.8568^{+0.0005}_{-0.0005}$	TESS Sector 67
$3248.7207^{+0.0083}_{-0.0099}$	Predicted
$3353.5820^{+0.0086}_{-0.0105}$	Predicted
$3458.4552^{+0.0073}_{-0.0091}$	Predicted
$3563.3545^{+0.0064}_{-0.0083}$	Predicted
$3668.2126^{+0.0003}_{-0.0003}$	JWST & TESS Sector 87
$3773.0616^{+0.0099}_{-0.0116}$	Predicted
$3877.9412^{+0.0005}_{-0.0005}$	TESS Sector 94
$3982.8322^{+0.0082}_{-0.0102}$	Predicted
$4087.7172^{+0.0099}_{-0.0125}$	Predicted
$4192.5741^{+0.0094}_{-0.0119}$	Predicted
$4297.4333^{+0.0085}_{-0.0107}$	Predicted
...	...

Note. H23 is M. J. Hobson et al. (2023). This table is truncated for brevity. The full table including predictions of transit times through 2040 December 31, UTC is available in machine-readable form.

(This table is available in its entirety in machine-readable form in the online article.)

Table 5
Prior and Posterior Distributions from Updated TTV Modeling Including New TESS and JWST Data

Parameter	Prior	Posterior
M_b (M_J)	$\mathcal{N}(0.169, 0.025)$	0.170 ± 0.020
M_c (M_J)	$\mathcal{U}(0.0, 5.0)$	0.261 ± 0.005
P_b (days)[a]	$\mathcal{U}(103.8540, 105.8540)$	104.869 ± 0.001
P_c (days)[a]	$\mathcal{U}(268.690, 278.69)$	$274.769^{+0.144}_{-0.141}$
$\sqrt{e_b}\cos(\omega_b)$	$\mathcal{U}(-0.7, 0.7)$	0.136 ± 0.012
$\sqrt{e_c}\cos(\omega_c)$	$\mathcal{U}(-0.7, 0.7)$	0.135 ± 0.013
$\sqrt{e_b}\sin(\omega_b)$	$\mathcal{U}(-0.7, 0.7)$	0.294 ± 0.008
$\sqrt{e_c}\sin(\omega_c)$	$\mathcal{U}(-0.7, 0.7)$	0.364 ± 0.007
e_b	Derived	0.105 ± 0.003
e_c	Derived	0.151 ± 0.003
ω_b	Derived	65.1 ± 2.3
ω_c	Derived	69.7 ± 2.1
T_{0_b} (BJD−2 458 300)[b]	$\mathcal{U}(8.5683, 113.3683)$	60.999 ± 0.001
T_{0_c} (BJD−2 458 300)[b]	$\mathcal{U}(7.43, 281.03)$	$160.741^{+0.685}_{-0.679}$

Notes. $\mathcal{N}(a, b)$ is a Gaussian distribution with mean a and standard deviation b. The posterior values are reported as the median, with uncertainties given by the 16th and 84th percentiles.

[a] We caution that the period values in this table should never be used to predict future transits in the TOI-199 system. These are approximations of the mean orbital period during the TTV simulation window. Using the period and T_0 values listed here to predict transits beyond the simulation window can result in errors much larger than the TTV amplitude shown in Figure 11. For transit timing predictions through 2040, see Table 4.

[b] The T_0 times listed here are a re-parameterization of the osculating mean anomaly (M_0) at the starting time of the simulation (BJD 2 458 262.350), and do not represent true transit times.

free parameter) with parameters initialized from the best-fit solution of M. J. Hobson et al. (2023), and ran the MCMC for 50,000 steps, discarding the first 20,000 steps as burn-in and ensuring convergence by verifying that each parameter reached more than 50 autocorrelation lengths in the MCMC.

Our updated TTV model including the new JWST data and three additional TESS transits produced results for the masses of TOI-199 b and c consistent within 2σ with the results of M. J. Hobson et al. (2023). Our complete TTV model results are listed in Table 5. Our derived mass for TOI-199 b is identical to that reported by M. J. Hobson et al. (2023), and therefore our atmospheric inferences are unaffected. Meanwhile, our new results improve the precision on the mass of TOI-199 c by approximately 50%, and reduce the uncertainty in the eccentricity by more than a factor of 3 for both planets. Our updated model prefers a larger orbital eccentricity for TOI-199 c (0.151 ± 0.003, compared to $0.096^{+0.008}_{-0.009}$ from M. J. Hobson et al. 2023), and a slightly larger mean orbital period for TOI-199 c, though still within the conservative habitable zone. Our updated TTV model also yields significantly different ω values for both planets, indicating nearly aligned longitudes of periastron for TOI-199 b and c, compared to the nearly anti-aligned ω values from the original fit of M. J. Hobson et al. (2023). We see two possible reasons for these changes. The first is simply the addition of new high-precision data improving the accuracy of the TTV fit, especially since there are now 14 total TTV points for a 10-parameter model, which makes the TTV solution less poorly constrained than the original 11 point dataset. The second is the difference in parameterization choice for e, ω, and M_0 which M. J. Hobson et al. (2023) samples directly and uses narrow priors defined by initial test runs, but we re-parameterize these quantities using transformations that reduce the correlations between e, ω, and M_0 and avoid convergence issues for circular parameters as suggested by previous TTV model comparisons (e.g., J. Eastman et al. 2013; E. Agol et al. 2021; M. Greklek-McKeon et al. 2025a), and we use wide uniform priors with one MCMC sampling until convergence is reached.

The eccentricity of TOI-199 b is not large enough to affect its transit shape (M. J. Hobson et al. 2023), but precise constraints on its e and ω values may be relevant for future eclipse observations. Given the shift in best-fit e and ω values when increasing the total data volume from 11 to 14 transits, these best-fit values may still change when more data are available. At the time of this writing, TESS is scheduled to re-observe the TOI-199 system in September, October, and December of 2025, in sectors 96, 97, and 98, respectively. New TTV fits with additional transits from these sectors may be able to further refine the mass of TOI-199 c and the orbital parameters for both planets. We list the predicted transit times for TOI-199 b through 2040 December 31 from our best-fit TTV model in Table 4 to aid in planning future observations of this system. Our predicted transit times for planet c do not show any transit events in the TESS data, supporting the

conclusion of M. J. Hobson et al. (2023) that the planet does not transit.

6. Discussion and Conclusions

6.1. Atmospheric Chemistry

TOI-199 b occupies a temperature regime that bridges the well-studied populations of hot Jupiters and solar system giants, allowing us to probe distinctive atmospheric chemistry not observed in either extreme. Unlike in hot Jupiters, where thermal chemistry often favors CO/CO_2 over CH_4 and NH_3 is largely dissociated, or cold giants, where CH_4 and NH_3 are stable but H_2O is depleted due to condensation, the chemical composition of TOI-199 b's atmosphere may provide a more complete census of the basic elemental abundance of the planet. Additional minor species from thermo- and photochemistry reflects a delicate balance between photochemical processes and the strength of vertical mixing.

Taking methane as a proxy for the bulk carbon abundance and thus metallicity (M. Asplund et al. 2009), our constraints from Table 2 correspond to an atmospheric metallicity of $C/H = 13^{+78}_{-12}\times$ solar (or $[C/H] = 1.11^{+0.85}_{-1.15}\times$ solar). However, we consider the high end of this range (i.e., $\gtrsim$50 $\times$ solar) to be disfavored because our photochemical models predict that at high metallicity, CO would overtake CH_4 as the dominant carbon carrier, which is inconsistent with our measured upper limits on CO and CO_2. For the same reasoning based on the CO upper limit, our models also disfavor internal temperatures much larger than 50 K.

Unlike in cooler gas giants, H_2O in the atmosphere of TOI-199 b is expected to be retained in the gaseous phase. Although we lack a direct detection, our H_2O upper limit constraint is within 1σ of the CH_4 abundance. Since H_2O is likely the dominant oxygen carrier in the atmosphere, a measured CH_4/H_2O ratio could provide precise constraints on the atmospheric C/O ratio.

The temperate regime of TOI-199 b makes its nitrogen chemistry especially sensitive to ongoing disequilibrium processes. In thermochemical equilibrium, the dominant nitrogen carrier is predicted to be NH_3, but with TOI-199 b's insolation, strong UV irradiation drives active photodissociation of both NH_3 and N_2, supplying nitrogen for HCN formation. This is in contrast to the Jovian atmosphere, where such photochemical processes result in the formation of hydrocarbons instead of HCN (G. R. Gladstone et al. 1996; J. Moses et al. 2005; R. Hu 2021). The strength of vertical mixing determines the relative importance of photochemistry: efficient vertical mixing in the deep atmosphere quenches NH_3 at higher pressures, increasing the supply of NH_3 to the observable atmosphere. Meanwhile, low K_{zz} values in the upper atmosphere, typical of solar system giants, allow photochemistry to dominate, potentially leading to the conversion of most NH_3 to HCN in the observable atmosphere. Complicating this interpretation, increased internal temperatures would reduce the abundance of both NH_3 and HCN. Thus, a reduced or absent NH_3 abundance could indicate either weak vertical transport or increased internal temperatures. Breaking this degeneracy requires constraints on the HCN/NH_3 ratio, together with major oxygen carriers such as CO or CO_2.

In addition, TOI-199 b's climate allows OCS to be more abundant than SO_2. The basic chemical pathway is similar to that described in R. Hu et al. (2025). Sulfur originates from the deep atmosphere in the form of H_2S, which dissociates into H_2 and S. Atomic sulfur then reacts with CO to form OCS. Subsequently, the CH_3 radical abstracts sulfur from OCS to produce CH_3S, which acts as a catalyst for the formation of CH_3SH. Both OCS and CH_3SH remain stable within the observable region of the atmosphere. Although OCS is not definitely detected through its 4.8 μm feature in the current data, our forward model predictions of OCS for enhanced metallicity agree well with the retrieved median and upper limit. OCS detection in TOI-199 b may provide a distinctive chemical fingerprint of temperate gas giants that is not observed in the temperature extremes of either solar system giants or hot Jupiters.

6.2. Follow-up Observations

High-precision observations will be essential to break the degeneracies between metallicity, C/O ratio, and vertical mixing, yielding crucial insights into the formation history and atmospheric dynamics of TOI-199 b and similar temperate giant planets.

HST GO program 17605 aimed to measure the transmission spectrum of TOI-199 b with WFC3/G141, targeting CH_4, NH_3, and H_2O. However, the HST observation was scheduled based on the period and zero-phase values currently listed on the NASA Exoplanet Archive (M. J. Hobson et al. 2023), without accounting for TTVs, which caused the observation to miss the transit (private communication). We caution against using the period or T_0 values in M. J. Hobson et al. (2023) or in this paper to schedule future transit observations, since that can result in errors much larger than the TTV amplitude. Instead, we recommend to use Table 4, which lists predicted transit times through 2040 December 31.

JWST is currently scheduled to observe two additional transits of TOI-199 b with NIRSpec to probe the 3–5 μm region (GO 7188, L. Acuna et al. 2025). Section 4 has shown the modeled transmission spectrum of TOI-199 b for two end-member nitrogen scenarios, anchored by the current data: (i) a Jupiter-like K_{zz} value with 10$\times$ solar metallicity, where HCN could be the main nitrogen carrier, and (ii) a hot Jupiter-like K_{zz} value, where NH_3 dominates. HCN and NH_3 both absorb near 3.0 μm, making them indistinguishable in the current data and limiting constraints on K_{zz}. However, we perform mock retrievals using our measured NIRSpec/G395H transmission spectrum, scaling the uncertainties down by a factor of six to emulate the precision expected from two transits with no WATA-related systematics. Under these conditions, the abundances of HCN and NH_3 could be constrained to $\sim$0.2–0.5 dex precision if they are present in the atmosphere at VMRs of $\sim 10^{-3}$. Such measurements would not only help determine the vertical mixing regime of this planet, but also constrain the photochemical production mechanisms of HCN (from its mixing ratio).

Such data would also constrain species like CH_4 and CO_2 to $\sim$0.1 and $\sim$0.2 dex precision assuming VMRs of $\sim 10^{-2}$ and $\sim 10^{-4}$, respectively. This will enable obtaining a comprehensive picture of the planet's C, N, and O inventories, and therefore precise measurements of the planet's metallicity and the elemental ratios C/O and N/O, which may hold clues to the planet's formation history (K. I. Öberg et al. 2011; D. Turrini et al. 2021; E. Pacetti et al. 2022).

If hazes are present in the atmosphere of TOI-199 b, future observations at shorter wavelengths could help distinguish their composition. While the three haze prescriptions explored

in this work are all consistent with the current spectrum in 3–5 μm, observations spanning 0.6–3 μm (e.g., with NIRISS/SOSS or NIRSpec's G235 gratings) would help break degeneracies between clouds and tholin/organic hazes through their differing spectral slopes.

The detection of CH_4 in TOI-199 b is consistent with the emerging trend that temperate ($T_{eq} \lesssim 400$ K) low-mean-molecular-weight atmospheres display spectral features in transmission spectroscopy (J. Brande et al. 2024; N. Madhusudhan et al. 2023; B. Benneke et al. 2024; R. Hu et al. 2025), with super-puffs as notable exceptions likely due to high-altitude hazes and/or circumplanetary rings (M. K. Alam et al. 2022; J. E. Libby-Roberts et al. 2026). However, TOI-199 b is the only planet in this list with a mass comparable to that of Jupiter. Ongoing JWST observations of similar long-period planets will not only test whether this trend extends across the gas giant population (J. Fortney et al. 2023; B. Cassese et al. 2026), but also begin to constrain their vertical mixing and photochemical processes, paving the way for a new era of atmospheric studies of temperate planets.

Acknowledgments

This work is based on observations made with the NASA/ESA/CSA James Webb Space Telescope. The data were obtained from the Mikulski Archive for Space Telescopes at the Space Telescope Science Institute, which is operated by the Association of Universities for Research in Astronomy, Inc., under NASA contract NAS 5-03127 for JWST. These observations are associated with program #5177. Support for this program was provided by NASA through a grant from the Space Telescope Science Institute under NASA contract NAS 5-03127. Part of this research was carried out at the Jet Propulsion Laboratory, California Institute of Technology, under a contract with the National Aeronautics and Space Administration (80NM0018D0004). Part of the high-performance computing resources used in this investigation were provided by funding from the JPL Information and Technology Solutions Directorate.

Data Availability

The JWST data used in this work are publicly available in the Mikulski Archive for Space Telescopes (MAST) at 10.17909/wbrk-af94. The transmission spectra and predicted transit times presented in this work are available on Zenodo: 10.5281/zenodo.17653116.

Appendix A
Atmospheric Retrievals Supplemental Information

Figure A1 shows the VMR posterior distributions from the `Aurora` retrievals on the different data reductions.

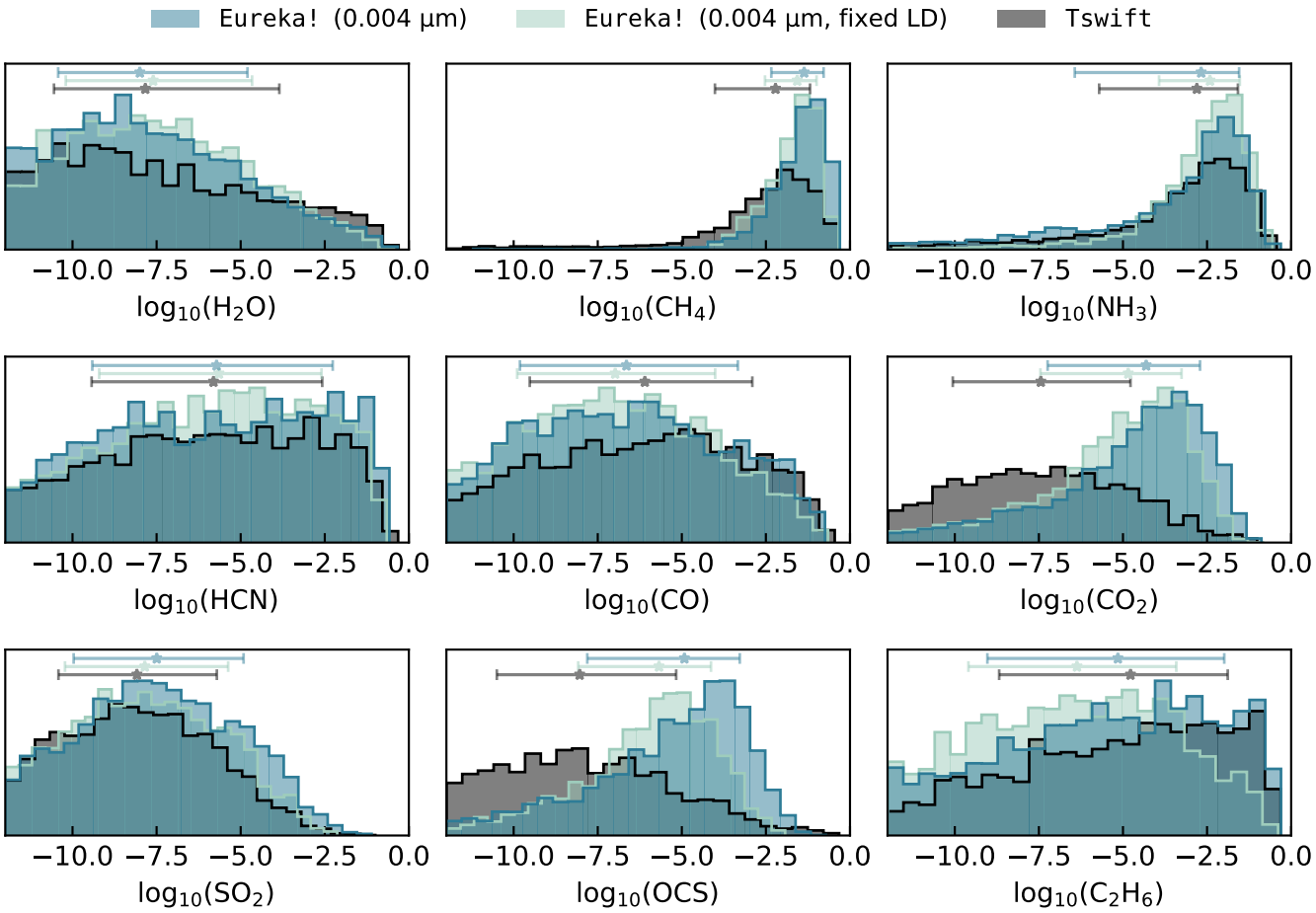


Figure A1. Same as Figure 6 but for `Aurora`.

Appendix B
Self-consistent Model Supplemental Information

EPACRIS-Climate solves for the 1D radiative-convective equilibrium using the improved 1D two-stream radiative solver (K. Heng et al. 2018). Here, the temperature-pressure (TP) profiles were computed assuming chemical equilibrium abundances for solar and enhanced metallicity cases (M/H = 10, corresponding to 10 times solar metallicity), as well as for solar and super-solar C/O ratios (0.59 and 1.1). The solar elemental abundances were taken from M. Asplund et al. (2021). We assumed full heat redistribution ($f = 0.25$), a null Bond albedo, and internal temperatures of $T_{\rm int} = 50$ K and $T_{\rm int} = 150$ K. To calculate the lapse rate, we employed the multi-component pseudo-adiabat equation derived by R. J. Graham et al. (2021). We included the opacities of all major expected species: H_2O, NH_3, CH_4, SO_2, CO_2, CO, H_2S, NO_2, NO, N_2, O_2, OH, HO_2, HCN, OCS, O_3, C_2H_6, CH_2O_2, HNO_3, N_2O, C_2H_2, C_2H_4, H_2CO, and H_2O_2, as well as collision-induced absorbers H_2–H_2, H_2–He, H_2–H, H_2–N_2, N_2–N_2, and CO_2–CO_2. The sources for the different opacities are the same as those listed in Section 3.1. We used the PHOENIX (T. O. Husser et al. 2013) stellar spectrum for all forward models. The resulting TP profiles for C/O = 0.59 are shown in Figure B1. The TP profiles for C/O = 1.1 did not show substantial differences and are therefore not shown.

Figure B1 also shows the adopted eddy diffusion coefficient profiles (K_{zz}) in our photochemical models. Notionally, we assumed K_{zz} to be constant in the convective region determined by the radiative-convective calculations ($K_{zz} = 10^6$ cm^2 s^{-1}) and the deeper atmosphere ($K_{zz} = 10^8$ cm^2 s^{-1}). The convective region value of 10^6 cm^2 s^{-1} was estimated to be comparable to planets with a similar $T_{\rm eq}$ based on X. Zhang & A. P. Showman (2018). The deep atmosphere value of 10^8 cm^2 s^{-1} was derived by the mixing-length theory (e.g., C. Visscher & J. I. Moses 2011) and is consistent with the GeH_4 tracer observations for Jupiter (D. Wang et al. 2016; G. L. Bjoraker et al. 2018).

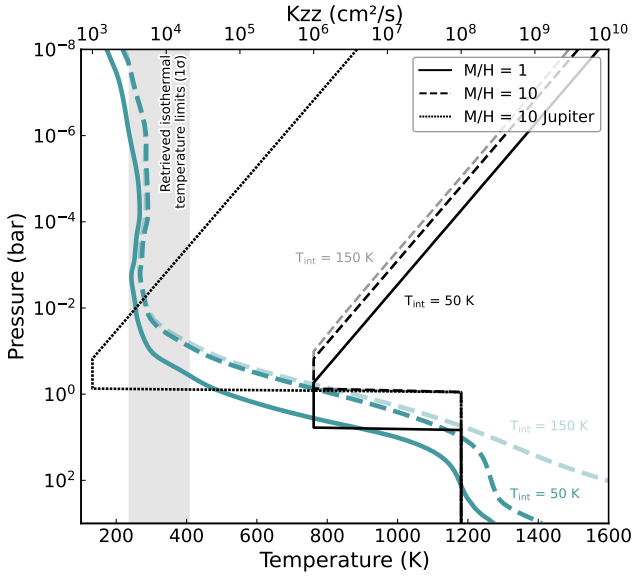


Figure B1. TP profiles (teal curves) and eddy diffusion profiles (K_{zz}, black curves) for TOI-199 b. Solid curves represent solar metallicity cases (M/H = 1), whereas dashed curves are for enhanced metallicity (M/H = 10). Faint curves represent the case with increased internal temperature. The dotted K_{zz} profile represents a Jupiter-like mixing case. The gray region indicates the retrieved 1σ temperature limits obtained from ExoTR retrievals.

However, recent work suggests that Jupiter's deep interior K_{zz} should be lower than this value according to 1D–2D coupled approaches (J. Yang et al. 2026), suggesting caution when adopting deep interior K_{zz} values. For comparison, we also ran models with a Jupiter-like K_{zz} profile, where K_{zz} is reduced to 10^3 cm^2 s^{-1} in the convective region (G. R. Gladstone et al. 1996). For both cases, K_{zz} was assumed to increase with the inverse square root of pressure above the convective region (R. S. Lindzen 1981) as implemented in R. Hu (2021). Finally, for further comparison, we consider another set of cases where a uniform K_{zz} is adopted throughout the atmosphere, with values ranging from 10^4 to 10^8 cm^2 s^{-1}, as these are typical assumptions for hot Jupiter studies (X. Zhang & A. P. Showman 2018).

Using the TP and K_{zz} profiles described above, we ran a suite of photochemical simulations with EPACRIS-Chemistry (J. Yang & R. Hu 2024a), adopting the chemical network of J. Yang & R. Hu (2024b), R. Hu et al. (2025), J. Yang (2025; 99 species and 2024 reactions in total), and the same PHOENIX stellar spectrum as described previously. We note that PHOENIX models typically underestimate UV flux (P. R. Behr et al. 2023), which may lead to slightly conservative estimates of photodissociation rates affecting photochemically produced species.

To generate the corresponding transmission spectra, we used the radiative-transfer code petitRADTRANS[13] (P. Mollière et al. 2019, 2020). Spectra were computed at a resolving power of $\lambda/\Delta\lambda = 1000$; although the figures display binned versions for clarity, the full-resolution spectra were used to compute χ^2 values for all forward models. For the reference pressure defining the radius of the planet we used $P_0 = 1$ bar. Most molecular opacities in petitRADTRANS were taken from the ExoMol database[14] (K. L. Chubb et al. 2021). A complete list of opacities and their line-list sources is provided in Table A.1 of M. Zilinskas et al. (2025).

ORCID iDs

Aaron Bello-Arufe https://orcid.org/0000-0003-3355-1223
Renyu Hu https://orcid.org/0000-0003-2215-8485
Mantas Zilinskas https://orcid.org/0000-0002-8749-823X
Jeehyun Yang https://orcid.org/0000-0002-1551-2610
Armen Tokadjian https://orcid.org/0000-0002-4675-9069
Luis Welbanks https://orcid.org/0000-0003-0156-4564
Guangwei Fu https://orcid.org/0000-0002-3263-2251
Michael Greklek-McKeon https://orcid.org/0000-0002-0371-1647
Mario Damiano https://orcid.org/0000-0002-1830-8260
Jonathan Gomez Barrientos https://orcid.org/0000-0002-0672-9658
Heather A. Knutson https://orcid.org/0000-0002-5375-4725
David K. Sing https://orcid.org/0000-0001-6050-7645
Xi Zhang https://orcid.org/0000-0002-8706-6963

References

Acuna, L., Berardo, D., Espinoza-Retamal, J. I., et al. 2025, All you need is Love numbers: simultaneous measurement of the oblateness and

[13] http://gitlab.com/mauricemolli/petitRADTRANS; version 2 was used for this work
[14] https://www.exomol.com/

atmospheric composition of a warm gas giant Cycle 4, ID. #7188, JWST Proposal
Agol, E., Dorn, C., Grimm, S. L., et al. 2021, PSJ, 2, 1
Airapetian, V., Glocer, A., Gronoff, G., Hebrard, E., & Danchi, W. 2016, NatGe, 9, 452
Alam, M. K., Kirk, J., Dressing, C. D., et al. 2022, ApJL, 927, L5
Alderson, L., Wakeford, H. R., Alam, M. K., et al. 2023, Natur, 614, 664
Ali-Dib, M. 2017, MNRAS, 467, 2845
Asplund, M., Amarsi, A. M., & Grevesse, N. 2021, A&A, 653, A141
Asplund, M., Grevesse, N., Sauval, A. J., & Scott, P. 2009, ARA&A, 47, 481
Barber, R. J., Strange, J. K., Hill, C., et al. 2014, MNRAS, 437, 1828
Batalha, N. E., Mandell, A., Pontoppidan, K., et al. 2017, PASP, 129, 064501
Behr, P. R., France, K., Brown, A., et al. 2023, AJ, 166, 35
Beichman, C. A., Giles, H. A. C., Akeson, R., et al. 2018, AJ, 155, 158
Bell, T., Ahrer, E.-M., Brande, J., et al. 2022, JOSS, 7, 4503
Bell, T. J., Welbanks, L., Schlawin, E., et al. 2023, Natur, 623, 709
Bello-Arufe, A., Damiano, M., Bennett, K. A., et al. 2025, ApJL, 980, L26
Benneke, B., Roy, P.-A., Coulombe, L.-P., et al. 2024, arXiv:2403.03325
Birkmann, S. M., Ferruit, P., Giardino, G., et al. 2022, A&A, 661, A83
Bjoraker, G. L., Wong, M. H., de Pater, I., et al. 2018, AJ, 156, 101
Brande, J., Crossfield, I. J., Kreidberg, L., et al. 2024, ApJL, 961, L23
Buchner, J., Georgakakis, A., Nandra, K., et al. 2014, A&A, 564, A125
Bushouse, H., Eisenhamer, J., Dencheva, N., et al. 2024, JWST Calibration Pipeline, v1.15.1, Zenodo, doi:10.5281/zenodo.12692459
Cassese, B., Kipping, D., Changeat, Q., et al. 2026, Aj, 171, 150
Chubb, K. L., Rocchetto, M., Yurchenko, S. N., et al. 2021, A&A, 646, A21
Cridland, A. J., van Dishoeck, E. F., Alessi, M., & Pudritz, R. E. 2019, A&A, 632, A63
Cridland, A. J., van Dishoeck, E. F., Alessi, M., & Pudritz, R. E. 2020, A&A, 642, A229
Damiano, M., Bello-Arufe, A., Yang, J., & Hu, R. 2024, ApJL, 968, L22
Deck, K. M., & Agol, E. 2016, ApJ, 821, 96
Eastman, J., Gaudi, B. S., & Agol, E. 2013, PASP, 125, 83
Ehrenreich, D., Lovis, C., Allart, R., et al. 2020, Natur, 580, 597
Espinoza, N., Fortney, J. J., Miguel, Y., Thorngren, D., & Murray-Clay, R. 2017, ApJL, 838, L9
Feinstein, A. D., Radica, M., Welbanks, L., et al. 2023, Natur, 614, 670
Feroz, F., Hobson, M. P., & Bridges, M. 2009, MNRAS, 398, 1601
Ford, E. B., Ragozzine, D., Rowe, J. F., et al. 2012, ApJ, 756, 185
Foreman-Mackey, D. 2018, RNAAS, 2, 31
Foreman-Mackey, D., Agol, E., Ambikasaran, S., & Angus, R. 2017, AJ, 154, 220
Foreman-Mackey, D., Hogg, D. W., Lang, D., & Goodman, J. 2013, PASP, 125, 306
Fortney, J., Bean, J. L., Fu, G., et al. 2023, C,N,O in a Temperate Jupiter: Bridging the Gap Between Solar-System and Exoplanet Atmospheres Cycle. 2, ID. #3235, JWST Proposal
Fortney, J. J., Visscher, C., Marley, M. S., et al. 2020, AJ, 160, 288
Fu, G., Espinoza, N., Sing, D. K., et al. 2022, ApJL, 940, L35
Fu, G., Welbanks, L., Deming, D., et al. 2024, Natur, 632, 752
Gladstone, G. R., Allen, M., & Yung, Y. 1996, Icar, 119, 1
Gordon, I. E., Rothman, L. S., Hargreaves, R. J., et al. 2022, JQSRT, 277, 107949
Graham, R. J., Lichtenberg, T., Boukrouche, R., & Pierrehumbert, R. T. 2021, PSJ, 2, 207
Grant, D., Lewis, N. K., Wakeford, H. R., et al. 2023, ApJL, 956, L29
Grant, D., & Wakeford, H. R. 2022, Exo-TiC/ExoTiC-LD: ExoTiC-LD v3.0.0, Zenodo, doi:10.5281/zenodo.7437681
Greklek-McKeon, M., Knutson, H. A., Levine, W. G., et al. 2025a, AJ, 170, 65
Greklek-McKeon, M., Vissapragada, S., Knutson, H. A., et al. 2025b, AJ, 169, 292
Hargreaves, R. J., Gordon, I. E., Rey, M., et al. 2020, ApJS, 247, 55
He, C., Radke, M., Moran, S. E., et al. 2024, NatAs, 8, 182
Heng, K., Malik, M., & Kitzmann, D. 2018, ApJS, 237, 29
Hess, M., Koepke, P., & Schult, I. 1998, BAMS, 79, 831
Hobbs, R., Shorttle, O., Madhusudhan, N., & Rimmer, P. 2019, MNRAS, 487, 2242
Hobson, M. J., Trifonov, T., Henning, T., et al. 2023, AJ, 166, 201
Holczer, T., Mazeh, T., Nachmani, G., et al. 2016, ApJS, 225, 9
Horne, K. 1986, PASP, 98, 609
Hu, R. 2021, ApJ, 921, 27
Hu, R., Bello-Arufe, A., Zhang, M., et al. 2024, Natur, 630, 609
Hu, R., Bello-Arufe, A., Tokadjian, A., et al. 2025, arXiv:2507.12622
Husser, T. O., Wende-von Berg, S., Dreizler, S., et al. 2013, A&A, 553, A6
Jakobsen, P., Ferruit, P., Alves de Oliveira, C., et al. 2022, A&A, 661, A80
Jeffreys, H. 1939, Theory of Probability (Oxford Univ. Press)
Jenkins, J. M., Twicken, J. D., McCauliff, S., et al. 2016, SPIE, 9913, 99133E
Kawashima, Y., & Ikoma, M. 2018, ApJ, 853, 7
Khare, B. N., Sagan, C., Arakawa, E. T., et al. 1984, Icar, 60, 127
Kipping, D. M. 2013, MNRAS, 435, 2152
Knutson, H. A., Charbonneau, D., Allen, L. E., et al. 2007, Natur, 447, 183
Kreidberg, L. 2015, PASP, 127, 1161
Lecavelier Des Etangs, A., Pont, F., Vidal-Madjar, A., & Sing, D. 2008, A&A, 481, L83
Libby-Roberts, J. E., Bello-Arufe, A., Berta-Thompson, Z. K., et al. 2026, AJ, 171, 221
Lindzen, R. S. 1981, JGRC, 86, 9707
Line, M. R., & Parmentier, V. 2016, ApJ, 820, 78
Line, M. R., Vasisht, G., Chen, P., Angerhausen, D., & Yung, Y. L. 2011, ApJ, 738, 32
Lithwick, Y., Xie, J., & Wu, Y. 2012, ApJ, 761, 122
MacDonald, R. J., & Madhusudhan, N. 2017, MNRAS, 469, 1979
Madhusudhan, N., Sarkar, S., Constantinou, S., et al. 2023, ApJL, 956, L13
Madhusudhan, N., & Seager, S. 2009, ApJ, 707, 24
Magic, Z., Chiavassa, A., Collet, R., & Asplund, M. 2015, A&A, 573, A90
Mancini, L., Lillo-Box, J., Southworth, J., et al. 2016, A&A, 590, A112
Mollière, P., Wardenier, J. P., van Boekel, R., et al. 2019, A&A, 627, A67
Mollière, P., Stolker, T., Lacour, S., et al. 2020, A&A, 640, A131
Mordasini, C., van Boekel, R., Mollière, P., Henning, T., & Benneke, B. 2016, ApJ, 832, 41
Moses, J., Fouchet, T., Bézard, B., et al. 2005, JGRC, 110, E08001
Murgas, F., Chen, G., Pallé, E., Nortmann, L., & Nowak, G. 2019, A&A, 622, A172
Nixon, M. C., Welbanks, L., McGill, P., & Kempton, E. M. R. 2024, ApJ, 966, 156
Öberg, K. I., Murray-Clay, R., & Bergin, E. A. 2011, ApJL, 743, L16
Ohno, K., & Fortney, J. J. 2023, ApJ, 946, 18
Pacetti, E., Turrini, D., Schisano, E., et al. 2022, ApJ, 937, 36
Parviainen, H., & Aigrain, S. 2015, MNRAS, 453, 3822
Richard, C., Gordon, I. E., Rothman, L. S., et al. 2012, JQSRT, 113, 1276
Rimmer, P. B., & Rugheimer, S. 2019, Icar, 329, 124
Rothman, L. S., Gordon, I. E., Barber, R. J., et al. 2010, JQSRT, 111, 2139
Salvatier, J., Wiecki, T. V., & Fonnesbeck, C. 2016, PeerJ Comp. Sci., 2, e55
Showman, A. P., Lewis, N. K., & Fortney, J. J. 2015, ApJ, 801, 95
Sing, D. K., Fortney, J. J., Nikolov, N., et al. 2016, Natur, 529, 59
Speagle, J. S. 2020, MNRAS, 493, 3132
Tennyson, J., Yurchenko, S. N., Al-Refaie, A. F., et al. 2016, JMoSp, 327, 73
Thorngren, D. P., Sing, D. K., & Mukherjee, S. 2026, ApJS, 283, 10
Tsai, S.-M., Innes, H., Lichtenberg, T., et al. 2021, ApJL, 922, L27
Tsai, S.-M., Lee, E. K., Powell, D., et al. 2023, Natur, 617, 483
Turrini, D., Schisano, E., Fonte, S., et al. 2021, ApJ, 909, 40
Underwood, D. S., Tennyson, J., Yurchenko, S. N., et al. 2016, MNRAS, 459, 3890
Visscher, C., & Moses, J. I. 2011, ApJ, 738, 72
Vuitton, V., Yelle, R., Klippenstein, S., Hörst, S., & Lavvas, P. 2019, Icar, 324, 120
Wang, D., Lunine, J. I., & Mousis, O. 2016, Icar, 276, 21
Welbanks, L., Bell, T. J., Beatty, T. G., et al. 2024, Natur, 630, 836
Welbanks, L., & Madhusudhan, N. 2019, AJ, 157, 206
Welbanks, L., & Madhusudhan, N. 2021, ApJ, 913, 114
Welbanks, L., & Madhusudhan, N. 2022, ApJ, 933, 79
Welbanks, L., Nixon, M. C., McGill, P., et al. 2026, NatAs, 10, 234
Wilzewski, J. S., Gordon, I. E., Kochanov, R. V., Hill, C., & Rothman, L. S. 2016, JQSRT, 168, 193
Winn, J. N., Holman, M. J., Torres, G., et al. 2008, ApJ, 683, 1076
Yang, J. 2025, RMG-generated Chemical Network for H2O-rich atmospheres (Yang and Hu, 2024), v1, Zenodo, doi:10.5281/zenodo.16750016
Yang, J., & Hu, R. 2024a, ApJ, 966, 189
Yang, J., & Hu, R. 2024b, ApJL, 971, L48
Yang, J., Hyder, A., Hu, R., & Lunine, J. I. 2026, PSJ, 7, 2
Yu, X., Moses, J. I., Fortney, J. J., & Zhang, X. 2021, ApJ, 914, 38
Yurchenko, S. N., Barber, R. J., & Tennyson, J. 2011, MNRAS, 413, 1828
Yurchenko, S. N., & Tennyson, J. 2014, MNRAS, 440, 1649
Zhang, X., & Showman, A. P. 2018, ApJ, 866, 1
Zilinskas, M., van Buchem, C. P. A., Zieba, S., et al. 2025, A&A, 697, A34